Recent Trends

in Charged Particle Optics and Surface Physics Instrumentation

Proceedings

of the 10th International Seminar,
held in Skalský dvůr near Brno, Czech Republic,
from May 22 to 26, 2006,
organized by
the Institute of Scientific Instruments AS CR and
the Czechoslovak Microscopy Society.

Edited by Ilona Müllerová

Published and distributed by the Institute of Scientific Instruments AS CR.
Technical editing by Marek Frank, printed by CCB, Brno.

ISBN 80-239-6285-X

PREFACE

The task to write a preface to the proceedings of a scientific meeting already tenth in succession surely makes one sitting and contemplating issues like usefulness of a given kind of meeting, tradition of this particular event, interest of the relevant eommunity in continuing this tradition and development of this interest in time, et cetera. In the case of 10th Recent Trends even more matters cross our mind: The first seminar was organized in an atmosphere overfilled with expectations, ten weeks before the Velvet revolution and with not more than five guests from the western abroad but really prominent ones. How much our local world has changed since that! And how much have altered our minds – surely more than what seventeen yeafs of the human life normally produce.

The idea underlying the meeting was untraditional and hence befitting the period of its birth: intention was to gather those dealing with similar problems just as in a family the members of which want to see each other regularly, to bring newly emerged youth with in order to initiate them into the community, to exchange meanings, of course, but more about unsolved questions than about momentarily acknowledged answers, and at last but surely not least, to spend together several nice days in pleasant surroundings. So created predestination projected itself into rather unusual elements of organisation. Instead of publicly dissipated announcements, personal invitations were addressed to personalities renowned in the given branch of science, supporting them to come together with their doctoral students. This really happened many times and even groups of up to elght persons were coming. In order to preserve stable impressions of the participants, starting from its third turn the event took place in the same hotel and schooling centre, situated midst the highlands in seclusion at a lake side. And the participants were gathered in the same room (the size of which traditionally limits the participation to fifty) and even the schedule always consisted of ten blocks of ninety minutes each. The Wednesday afternoon's walking trip closed with a dinner in some rustic inn, the Tuesday's open-air barbecue as well as the Thursday evening's concert - all this makes the Recent Trends an extremely traditionalistic event.

However, otherwise everything has kept changing, not excluding the atmosphere of scientific conferencing in general and of meetings organized for electron opticians and surface scientists in particular. In between the Czech science and scientists have entered the situation at least qualitatively identical with that faced by their foreign colleagues. And this situation, maybe under influence of mushroom growth in communication tools and media, has also changed in such a way that scientists have gradually lost a good deal of their enthusiasm for travelling and for gathering personally into groups of a moderate size. While the largest congresses seem to survive well, smaller meetings like ours suffer from problems with getting the overloaded scientists to a place even known to them as a quite pleasant one (what they always claimed). Well, once again Ilona has succeeded in gathering the assembly of participants on the traditionally excellent level. Do we want to continue again in two years? Let we discuss this during the meeting's breaks.

Allow me to believe that also this time the days spent at the Skalský dvůr will be pleasant and fruitful for everybody.

Luděk Frank

CONTENTS

PRACTICAL MEASURE FOR THE BRIGHTNESS OF ELECTRON SOURCES

J.E. Barth, M.S. Bronsgeest

Delft University of Technology
Lorentzweg 1, 2628 CJ, Delft, Netherlands
J.E.Barth@tudelft.nl

To characterize electron sources, usually the reduced differential brightness

$$B_{diff} = \frac{1}{V} \lim_{\delta A \to 0} \lim_{\delta \Omega \to 0} \frac{\delta I}{\delta A \delta \Omega} \qquad (1)$$

is given, with current δI, area δA solid angle $\delta \Omega$, and extraction voltage V.

However, when electron sources are used for probe formation, the differential brightness is not the relevant parameter:
In a scanning electron microscope the virtual source is imaged in the probe. The virtual source has a bell-shaped intensity profile. The differential brightness, being the brightness at the top of the source intensity profile, is therefore not applicable.

When sources are used for probe formation the only brightness with a real physical meaning, is the reduced brightness, as Crewe has pointed out [1]:

$$B = \frac{I'}{V \frac{\pi}{4} d_v^2} \qquad (2)$$

where I' is the angular current density, which is taken to be constant over a finite solid angle, and d_v is the diameter of the virtual source. However, Crewe does not give a definition of that 'diameter'. In order to have a **practical** brightness a practical definition is needed. A measure that assumes no particular shape of the source intensity profile is the diameter containing a fraction FC of the current $I'\Omega$ coming from the virtual source as seen from the extractor.
To complete the definition a choice has to be made for the value of FC. For a number of reasons we propose a fraction of 0.5. We consider this value most likely to be generally acceptable to the charged particle optics community.

We have derived the relation of the **practical** brightness to the **differential** brightness for the particular case of the Schottky source.

For Schottky sources the reduced differential brightness is (e.g. [2])

$$B_T = \frac{1}{V} \frac{j}{\pi kT} \qquad (3)$$

with j the cathode current density, k the Boltzmann constant, and T for temperature. The virtual source has a Gaussian intensity profile [2]. The practical brightness is

$$B = 1.44 B_T \,. \tag{4}$$

This differs significantly from the usual assumption that the differential brightness can be used for probe size calculations. [3]

[1] A.V. Crewe, Ch. 10 in 'Handbook of Charged Particle Optics', ed. J. Orloff, CRC Press (1997), p. 406

[2] J. Worster, J. Phys. D 2 (1969) 889

[3] P. Kruit, M. Bezuijen and J.E. Barth, J. Appl. Phys. 99 (2006) 024315

PURIFICATION OF PLATINUM AND GOLD STRUCTURES AFTER ELECTRON-BEAM-INDUCED DEPOSITION

A. Botman, J. J. L. Mulders, R. Weemaes and S. Mentink

(A.B., S.M.) Philips Research Laboratories, High Tech Campus 34, 5656AE Eindhoven, The Netherlands. Electronic Mail: aurelien.botman@philips.com.
(R.W.) Philips Research Laboratories, High Tech Campus 11, 5656AE Eindhoven, The Netherlands.
(J.M.) FEI Electron Optics, Achtseweg Noord 5, 5651GG Eindhoven, The Netherlands.

The technique of electron-beam-induced deposition (EBID) [1], when performed with organic precursors, typically results in a relatively low metal content due to the partial decomposition of the organic precursor, leaving carbon rich remnants in the deposition [2]. Solutions investigated elsewhere have included annealing in-situ after [3] or during [4] deposition, or deposition in reactive environments [5]. These two approaches have apparently not yet been combined.

We described a method applied to noble-metal structures deposited using EBID, which consisted of a post-treatment step of heating in a reactive atmosphere of oxygen, whereby the amount of carbon in the structure is strongly reduced [6]. As a result we have been able to increase the purity of platinum deposits from 15 at% to nearly 70 at%, and gold similarly from 8 at% to nearly 60 at%.

The resistivity of these structures has also been improved by up to 4 orders of magnitude, to achieve $(1.4 \pm 0.2) \times 10^4$ μOhm.cm in the case of platinum. Furthermore, STEM analysis of the treated structures has shown formation of crystalline material (Figure 1).

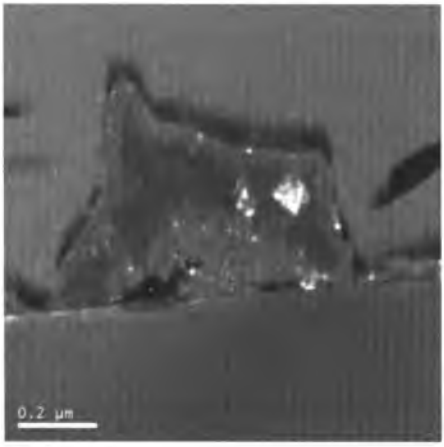

Figure 1. Dark-field STEM image of one platinum structure in cross-section. This sample was treated at 500°C in O_2. Uniformly dark or light areas have the same crystallographic orientation, indicating the presence of crystalline grains. Untreated samples appeared uniformly grey (signature of amorphous material).

[1] Willem F. van Dorp, Bob van Someren, Cornelis W. Hagen, Pieter Kruit, and Peter A. Crozier, "Approaching the resolution limit of nanometer-scale electron beam-induced deposition", *Nano Letters*, **5(7)**:1303-1307, (2005).

[2] D. Beaulieu, Yong Ding, Z. L. Wang, and W. J. Lackey, "Influence of process variables on electron beam chemical vapor deposition of platinum", *J. Vac. Sci. Technol. B*, **23(5)**:2151-2159, (2005).

[3] Gian Carlo Gazzadi and Stefano Frabboni, "Fabrication of 5 nm gap pillar electrodes by electron-beam Pt deposition", *J. Vac. Sci. Technol. B*, **23(2)**:L1, (2005).

[4] H. W. P. Koops, C. Schoessler, A. Kaya, and M. Weber, "Conductive dots, wires, and supertips for field electron emitters produced by electron-beam induced deposition on samples having increased temperature", *J. Vac. Sci. Tecnhol. B*, **14(6)**:4105, (1996).

[5] Albert Folch, Javier Tejada, Christopher H. Peters, and Mark S. Wrighton, "Electron beam deposition of gold nanostructures in a reactive environment", *Appl. Phys. Lett.*, **66(16)**:2080, (1995).

[6] A. Botman, J. Mulders, R. Weemaes and S. Mentink, "Purification of platinum and gold structures after electron-beam-induced deposition", *(manuscript in preparation)*.

SIGNAL DETECTION WITH SEGMENTAL IONIZATION DETECTOR

P. Černoch[2], J. Jirák[1, 2]

[1]Institute of Scientific Instruments ASCR, Královopolská 147, 612 64 Brno, Czech Republic
[2]Department of Electrotechnology FEEC BUT, Údolní 53, 602 00 Brno, Czech Republic
xcerno07@stud.feec.vutbr.cz

The gaseous ionization detector [1] is often utilized for signal detection at a higher pressure in the specimen chamber of the environmental scanning electron microscope. We study the properties of halved segmental ionization detector with an electrode system consisting of four concentric electrodes divided into left and right halves, as seen in Fig. 1.

Each electrode of the detector can be connected to one of the three following options: a potential of 0 V to 500 V with signal detection, a potential of -500 V to 500 V without signal detection or a ground. The electrode system connection at signal detection by the left smallest electrode (A_L) at a voltage of 350 V while the right smallest electrode (A_R) is at a voltage of -200 V and all other electrodes are grounded is illustrated in Fig. 2. For this electrode system connection, electron trajectories in the electrostatic field in a vacuum simulated via program Simion 3D 7.0 is shown in Fig. 3a and the image of the semiconductor specimen is shown in Fig. 4a. Likewise, the electron trajectories simulation and the specimen image at the electrode system connection at signal detection by electrode A_L at a voltage of 350 V while electrode A_R is at a voltage of 350 V and all other electrodes are grounded are shown in Fig. 3b, 4b.

In the case of a negative voltage on the non-detection electrode, signal electrons emitted from the specimen are repelled by the non-detection electrode (A_R) and attracted by the detection electrode (A_L). This effect is observed as a brighter specimen image with symmetrical shadow and diffusion contrasts in Fig 4a. In the case of symmetrical voltages on the detection and the non-detection electrodes, signal electrons emitted from the specimen are divided symmetrically to the both electrodes A_L and A_R, therefore, the angle of the signal electrons detection by the detection electrode (A_L) manifest itself, as seen in 4b. The simulations correspond to the obtained specimen images, as illustrated in Fig. 3a and 3b.

According to the electron trajectories simulations and the specimen images, it is seen that the effect of change of contrast, shadow and diffusion, is possible to achieve not only by a change of detection electrode position but also by a change of voltages on non-detection electrodes influencing secondary electron trajectories.

This research is supported by project GACR No. 102/05/0886 and project MSM 0021630516.

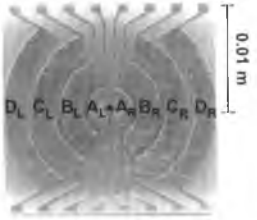

Fig. 1. Halved segmental ionization detector

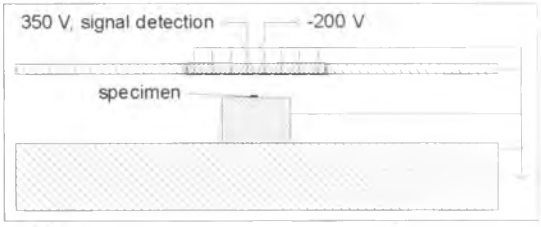

Fig. 2. The electrode system connection at signal detection by electrode A_L at voltage of 350 V; voltage of -200 V on electrode A_R; all other electrodes grounded

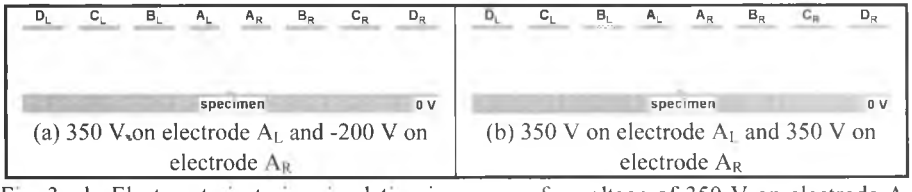

(a) 350 V on electrode A_L and -200 V on electrode A_R

(b) 350 V on electrode A_L and 350 V on electrode A_R

Fig. 3a, b. Electron trajectories simulation in vacuum for voltage of 350 V on electrode A_L and voltages of -200 V or 350 V on electrode A_R; other electrodes and specimen grounded: electron energy 5 eV; projection angle of electrons 0 to 180 degrees

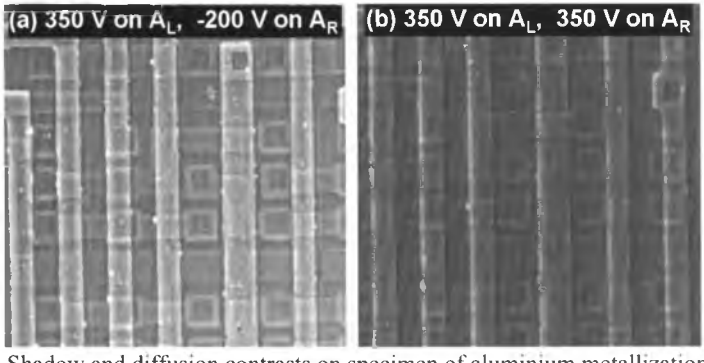

Fig. 4a, b. Shadow and diffusion contrasts on specimen of aluminium metallization on silicon substrate; signal detection by electrode A_L at voltage of 350 V; voltages of -200 V or 350 V on electrode A_R, other electrodes grounded; water vapors environment, 750 Pa, mag. 2000x

[1] Danilatos, G. D.: Theory of Gaseous Detector Device in the Environmental Scanning Electron Microscope. Sydney, Academic Press 1990, 103 p., ISBN 0-12-014678-9

[2] Toth, M., Daniels, D. R., Thiel, B. L., Donald, A. M.: Quantification of Electron-Ion Recombination in an Electron-Beam-Irradiated Gas Capacitor. Journal of Physics D. Vol. 35, 2002, p. 1796 – 1804

[3] Idaho National Engineering and Environmental Laboratory: Simion 3D 7.0. Bechtel BWXT Idaho, LCC, 1999

LOW VOLTAGE ELECTRON MICROSCOPE FOR BIOLOGICAL OBJECTS

A. Delong, P. Štěpán

Delong instruments, a. s.
Bulharská 48
612 00 Brno, Czech Republic

Understanding the three- dimensional structure of proteins and other particles (viruses, ribosomes, enzymes, DNA) is critical in determining how they perform their biological functions. The usually used technique of X-ray diffraction requires perfect crystals with approximately 10^{12} molecules. Electron microscopy should be superior to X-ray diffraction and 200-400kV transmission electron microscopes (TEM) are used for obtaining satisfactory information. But today's microscopes must overcome various obstacles connected with the properties of biological objects. It is first of all very low contrast and sensibility to radiation damage. The result of this fact is the necessity of elaboration of high quantity of very noisy pictures (1-100k) to get satisfactory results.
It seems that the low voltage transmission electron microscope developed specifically for application in biology will be more suitable for solving from above introduced task first of all due to a much higher contrast. We shall compare the main parameters of two different TEMs- 200kV TEM dedicated for biological applications and a 5kV low voltage TEM.

Contrast
The usual objects are so thin that all impinging electrons in both microscopes are transmitted. We will now compare how the standard object (10nm thick specimen composed from material with R= 1g/cm and a diameter greater than the resolution of the microscope) influences the trajectories and the energy of transmitted electrons. The results of calculations are presented on the figure 1.[1]. There are in principle three kinds of electrons in the transmitted beam
electrons which were transmitted without any interaction
electrons which were elastically scattered. Their trajectories were changed due to deflection in electrical field of the atomic nucleus and its electron shell. Electrons falling upon the rim of a physical aperture are excluded from the beam and appear to have been absorbed. This electrons produce contrast
Some electrons are deflected by direct interaction with atomic electrons. A measurable amount of energy is transferred, and the resulting deflection together with energy loss is called inelastic scattering. If we compare the results of calculations in both microscopes we see that the contrast and the radiation damage are more favourable in the LVTEM.

Resolution
The resolution of 200kV TEM is 0.27nm approximately. The resolution of LVTEM is 2nm. The very low contrast of biological objects in 200kV TEM must be increased by using the phase contrast. The necessary defocusing decreases the resolution to the value of 1 – 2nm.Nevertheless the correction of both mean aberrations (spherical and chromatic) can bring new possibilities for LVTEM. We decided to correct the spherical aberration by means of hexapol corrector and the chromatic aberration by means of inhomogeneous Wien filter. We used the proposal published by prof. Rose 17 years ago.[2] This proposal was never implemented, although its advantages are obvious. It is the rotational symmetry of both correctors and minimum of multipoles. Another advantage is the possibility to use the Wien filter alternatively as an electron energy loss spectrometer (EELS). The cross-section of the

C_SC_C corrected LVTEM is presented on the figure 2. The hole electron optical system is very short (180mm) and therefore not sensitive to vibrations and stray magnetic fields.

Radiation damage

First of all I would like to cite from the article of L.F.Drummy [3]. "A fundamental question that remains open is the quantitative variation in total inelastic scattering with decreasing electron energy. Observations of samples imaged in the LVTEM have given intriguing qualitative clues about how these interactions differ as the voltage is decreased. For example, for sufficiently thin specimens (10-20nm) it seems that there is a significant decrease in the inelastic scattering. Specifically, the images at low thickness are sharper and do not show the characteristic halos that are typical of chromatic aberration. With thick samples there is a loss of resolution and the halos characteristic of chromatic aberration become more obvious. "We observed the same properties of thin specimens when imaged in LVTEM. No theoretical foundation for this fact exists in the literature...

Conclusion

The LVTEM with its possibility to reach high contrast of biological objects without using heavy metals for staining is very promising device for studies in more native form. It seems to be logic in the situation when the contrast increased very significantly even in the case of very thin objects(1nm) to increase resolution too. Correction of objective aberrations by means of multipoles seems to be the best solution. The experiment is prepared, its result is of course uncertain. A simpler way is to decrease dimensions of the objective lens and or to use the hollow cone illumination. It seems to be possible to reach the resolution of 0.3nm which can be enough for majority of demands.

References

[1] E.Zeitler, G.F.Bahr: Quantitative Electron Microscopy, Armed Forces Institute of Pathology,Washington, D.C.1965, 946 p.
[2] H.Rose: Optik 84,3(1990) 91.
[3] L.F.Drummy, J.Yang, D.C.Martin: Ultramicroscopy 99(2004) 247.

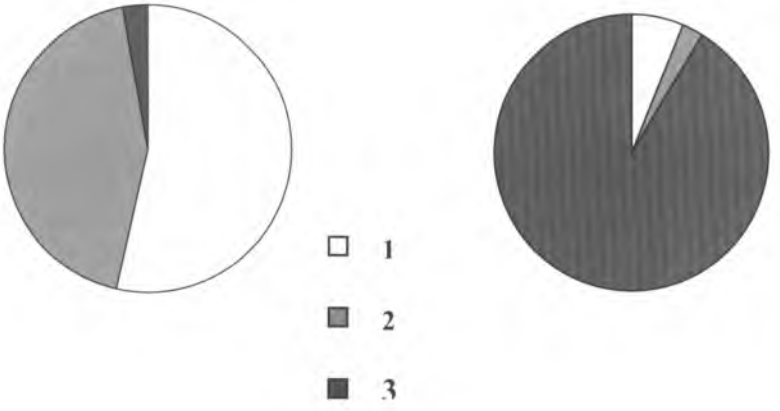

Figure 1: Quantitative distribution of electrons which transmitted the object with ρ=1g/cm3 and thickness t=10nm. 1 – elastically scattered ($\alpha>\alpha_{opt}$), 2 – not scattered and elastically scattered ($\alpha<\alpha_{opt}$), 3 – inelastically scattered.

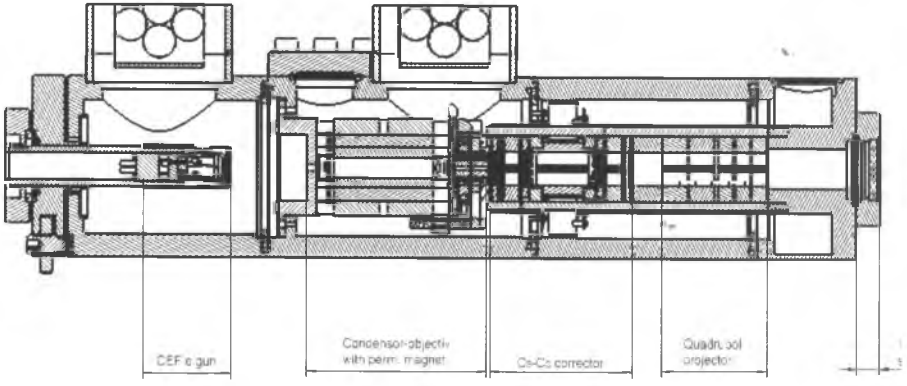

Figure 2: Cross-section of the electron optical column of C_sC_c corrected LVTEM

ELECTRON BEAM MICROMACHINING

L. Dupák*, M. Zobač

Institute of Scientific Instruments AS CR, Kralovopolská 147, 61264 Brno, Czech Republic
* E-mail: ldupak@isibrno.cz

Electron beam micromachining is a well-known technology used in various industrial applications [1]. It is based on the evaporation of material by intense electron beam [2]. The construction of the e-beam micromachining equipment may be similar to an e-beam welder, but it needs a high performance electron optical system to achieve very high power density in the focus of the beam (usually 100 times or higher). We have studied ability of a common e-beam welder to machine the materials like quartz glass, ceramics, plastics and metal sheets. The purpose of our experiments was to create holes as small as possible [3].

In micromachining, a short-pulse beam is used instead of a continuous beam. If a continuous beam is used, a lot of heat is supplied to the surrounding material. This has undesirable effects like growth of the diameter, deformation and material tension.

Pulse count	1	2	5	10	20
Depth (mm)	2.78	3.42	4.06	4.19	4.7
Diameter (mm)	0.32	0.34	0.39	0.43	0.48
Depth/dia ratio	8.7:1	10:1	10:1	9.7:1	9.8:1

Table 1. Dependence of hole dimensions on pulse count (beam current 1 mA).

In our first experiment, we have followed the growth of the hole in the material exposed to a series of the pulses (see Table 1). The highest growth of the hole dimensions was observed after the first pulse. The effect of the following pulses was decreasing with each step.

The effect of focus point position was determined in the next experiment. The beam pulses were counted until the beam passed through 0.9 mm thick quartz glass slide. The lowest number of the pulses was needed when the beam was focused exactly on the surface. But as seen in Fig. 2, the holes created by defocused beam had higher apical angle and lower minimal diameter.

The position of the minimal diameter is not located on the surface, but a small distance from it, sometimes more than 0.1 mm. This is probably caused by a burst of the evaporated material. The surface tension of the melted material then forms the narrow neck.

We have been able to create openings of 5 to 17 μm minimum diameter (measured by light microscope and scanning electron microscope – see Fig. 3). However, reproducibility of such

Fig. 1. Typical hole with expansion of the exit side of the hole (quartz thickness 0.9 mm).

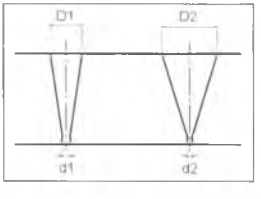

Fig. 2. Sketch of conical hole in dependence on focus. 1) focused on surface, 2) defocused.

Fig. 3: Figure of the exit side of the hole from SEM.

small holes is low because the melted material very often refills the opening. Subsequent pulse breaks through this barrier and creates a hole larger than the previous ones.

The deeper and wider openings are produced when higher beam current is applied (see Fig. 4 and Table 2), because the beam size in the focus increases, too.

Ceramics, due to their low thermal conductivity, are easy to machine. In 0.6 mm thick sample of white Al_2O_3 ceramic we were able to drill holes 150 μm wide on the beam impact side and less than 100 μm on the exit side. Unfortunately, some samples cracked.

We have tried drilling of stainless steel and titanium, being able to create holes of a diameter less than 100 μm in stainless steel (sheet thickness 0.05 mm and 1 mm) and 120 μm in titanium (sheet thickness 0.6 mm).

E-beam drilling of many different plastic materials was performed, mainly to test the experimental equipment with improved capability to keep the pressure in the electron gun high enough during machining of plastics. Polyethylene (PE) and polyamide (PA 6/G-oil) were easy to machine. The smallest hole diameter bored in PE was 50 μm (see Fig. 5) and 150 μm in PA.

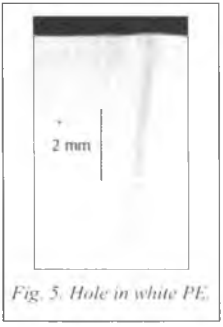

Fig. 5. Hole in white PE.

One of the practical applications of the presented technology was construction of quartz multi-atomizer for atomic absorption spectrometry. Important part of this device is quartz glass tube, 160 mm long, 7 mm in diameter with 0.7 mm thick wall. We successfully drilled 18 holes regularly distributed along its length.

Other application in which we used e-beam micromachining was creation of circular groove in a ceramic sphere. Into this groove, a thin-wall stainless steel capillary is inserted and glued (see Fig. 6.). The ceramic spheres were 8 and/or 5 mm in diameter. Diameters of the cuttings were 3, 2.5 and 2 mm.

i_S (mA)	0.2	0.3	0.5	0.8	1
Depth (mm)	0.82	1.34	2.01	2.3	2.78
Diameter (mm)	0.12	0.15	0.21	0.29	0.32
Depth/dia ratio	6.8	8.9	9.6	7.9	8.7

Tab. 2. Dependence of hole dimensions on beam current.

[1] http://www.steigerwald-eb.de/ (April 2006).

[2] A. Visser: Werkstoffabtrag Durch Elektronen und Photonenstrahlen, Blaue TH Reihe, Heft 104 (1972) Verlag «Technische Rundschau» im Hallwag Verlag, Bern und Stuttgart.

[3] L. Dupák: Diploma thesis. 2005 Brno [in Czech].

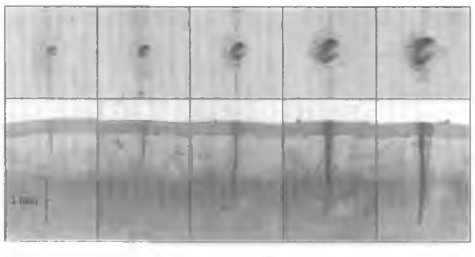
Fig. 4. Dependence of effects of a single pulse on beam current (as in Tab. 2.) Pulse length 50 ms.

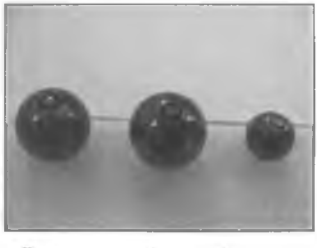
Fig. 6. Grooves in ceramic spheres (8 mm and 4 mm in diameter)

AN ENERGY ANALYSER FOR HARD X-RAY PHOTOELECTRON SPECTROSCOPY

M. Escher[1*], M. Merkel[1], J. R. Rubio-Zuazo[2,3], G. R. Castro[2,3]

[1]Focus GmbH, 65510 Hünstetten, Germany
[2]SpLine, Spanish CRG beamline at ESRF, Grenoble, France
[3]ICMM-CSIC Cantoblanco, Madrid, Spain
* m.escher@focus-gmbh.com

Introduction

Recently the interest in hard X-ray photoelectron spectroscopy (HAXPES) grew with the availability of high brilliant synchrotron beamlines [1].With the longer escape depth of the high energetic electrons HAXPES has the capability of probing bulk properties, buried layers or interfaces down to some tens of nanometers, which is not possible with the surface sensitive standard XPS.

Analyser

We developed an energy analyser, HV-CSA (High Voltage Cylinder Sector Analyser), for electron energies up to 15keV. It is the first commercially available analyser for that energy range. The analyser is based on a cylinder sector with 90° deflection [2], 300 mm slit-to-slit distance and an entrance lens with 50 mm sample distance. The result is a very compact design of the analyser that is easily integrated into a multi purpose experiment with different techniques. A low noise / low drift electronics is capable of continuous energy scans from 0 to 15keV with non-linear lens curves. The first analyser has been recently installed at the Spanish CRG beamline at the ESRF (Grenoble) at an end station where simultaneous surface X-ray diffraction is possible [3]. Fig. 1 shows a photograph of the analyser.

Fig.1: Photograph of the High Voltage Cylinder Sector Analyser HV-CSA

Entrance Lens

The entrance lens retards the high energetic electrons with a kinetic energy E_{kin} up to 15keV to the analyser's pass energy E_{pass} (typically 20..100eV) which results in retardation ratios $R = E_{kin}/E_{pass}$ up to 1000. To accept a large phase space at the analyser's entrance slit $E_{pass} A_{slit} \Omega_{analyser} = E_{kin} A_{sample} \Omega_{sample}$, the design goal was to have a large lateral magnification $M = \sqrt{A_{slit}/A_{sample}}$ which is also well adapted to a focussed synchrotron beam of typically 50µm diameter.

The entrance lens consists of a unipotential lens near the sample followed by a three element retardation stage. Its properties were calculated with direct ray-tracing using

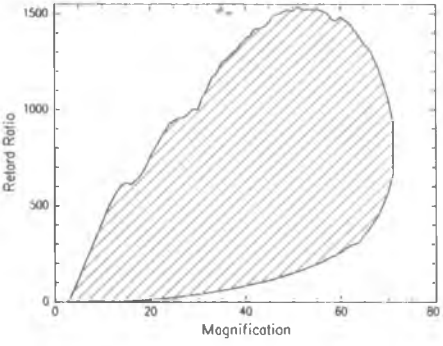

Fig. 2: Range of useable magnifications and retard rations of the entrance lens.

Simion 7.0. Lens voltage settings were found using Newton's method in three dimensions with respect to a given focus position, magnification and vanishing beam angle. Fig. 2 shows the range of retard ratios and magnifications where adequate lens voltages could be found.
The dependence of the lens transmission on the magnification has two limiting cases. For small magnifications the transmission space is restricted by the fixed solid angle accepted by the analyser $\Omega_{analyser} = R/M^2\,\Omega_{sample}$. The transmission will rise with M^2 up to the point where the lens entrance limits the angular acceptance. For large magnifications the intensity is cut by the entrance slit of analyser and the transmission drops with M^{-2}. Between these two limiting cases a constant transmission is expected. Fig. 3 shows the measured transmission dependence for a retardation of 200 using 10keV elastic electrons. The smooth transition between the three regions results from lens aberrations and spot aberrations of the e-gun used.

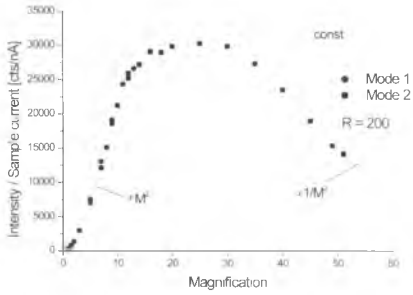

Fig. 3: Measured analyser transmission as a function of lens magnification. The peak intensity scaled to the measured sample current is shown for different magnifications. The dashed lines indicate the expected theoretical behaviour.

Results

First results with the HV-CSA were obtained using elastically scattered electrons of a 15keV RHEED-gun. Elastic peaks measured for different pass energies and the peak widths are shown in Fig. 4. The energy widths of the peaks follow the expected linear behaviour and are restricted to the intrinsic energy width of the electron gun of approx. 0.5eV. Using HeI excitation an analyser energy resolution of 40meV could be shown using the same electronics.

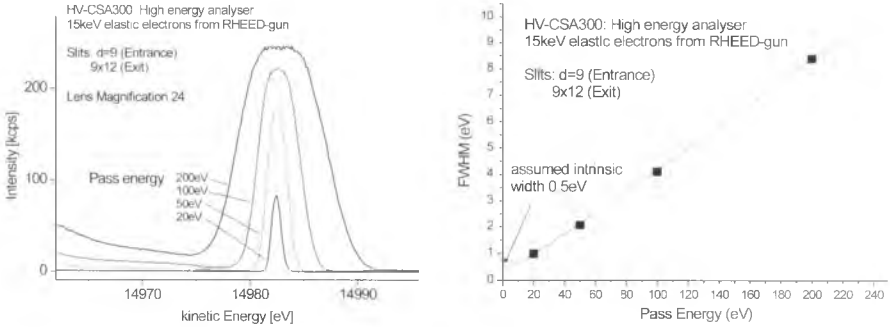

Fig 4: left: spectra of elastically scattered electrons from a 15keV e-gun for different E_{pass}
right: pass energy dependence of the measured energy widths.

[1] Proceedings of the HAXPES workshop in Nucl. Instrum. A, **547** (2005) 1-238
[2] J. Risley, Rev. Sci. Instrum. **43** (1972) 95
[3] J.R. Rubio-Zuazo, G.R. Castro, Nucl. Instrum. A, **547** (2005) 64-72

THE DOPANT CONTRAST – A CHALLENGE TO ELECTRON MICROSCOPY

L. Frank

Institute of Scientific Instruments ASCR, Královopolská 147, 61264 Brno, Czech Republic
ludek@isibrno.cz

The continuous reduction to feature dimensions in semiconductor structures enhances the need for high resolution imaging of doped patterns in plan views of substrates or on their cross-sections. In this way a tool is sought for checking the critical dimensions (CD) of the structures and, moreover, for two-dimensional profiling the spatial distribution of active dopants. Various surface-oriented electron microscopic methods have been used with varying success. The contrast levels are often achieved sufficient for CD measurements but detailed interpretation of images keeps being unclear and hence, irrespectively of some promising experiments [1,2], any reliable quantification of contrasts, enabling one to determine the local density of a dopant, remains for the future. This review aims at brief summarizing of achievements in this field.

Numerous of the attempts performed so far have relied upon imaging in the secondary electrons (SE). Great majority of studies reported the p-type Si brighter than the n-type and in discussions usually three possible emission-controlling factors were mentioned. These include the SE generation rate, influence of electrical fields below or even above the surface, and the passage through the surface potential barrier. All these factors are interconnected through differences in the energy band structures, determined by the types and densities of dopants. Older works ascribed the decisive role to the ionization potential, i.e. the surface barrier height, combined with above-surface "patch" fields balancing the local differences in the inner potential [3-8].

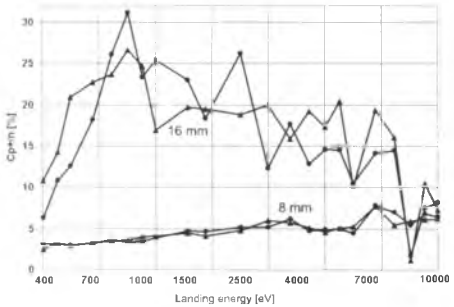

Figure 1: SE image contrast between the p-type (10^{19} cm^{-3}) patterns and n-type (10^{15} cm^{-3}) Si substrate, plotted versus the electron energy, as measured (two times) for working distances of 16 and 8 mm; reproduced from Ref. 15.

Further step was to admit that the surface conditions act not only via surface states but also the treatment and hence cleanliness play their roles. In particular, the carbon contamination together with silicon may form a planar junction of properties similar to a metal-semiconductor junction; then the balancing electric fields remain below the surface but still they provide explanation for at least a part of observations [9-11]. This conception was verified by covering a p/n structure with metals of different work functions, which led to mutually opposite contrasts [11,12]. As regards the surface barrier, its filtering action, similarly as that of the patch fields, concerns only the velocity component normal to the surface. This brings not only unequal flows surmounting the barrier but also the angular

distributions of the emission become differently modified [13,14], which in turn, in combination with angular acceptance range of the detector, may influence the contrast acquired [14,15] (see Fig. 1). An additional contrast-influencing factor has been revealed in the beam current (or electron dose) [16,12].

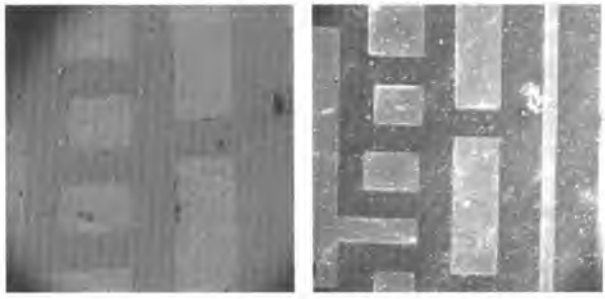

Figure 2: P-type patterns (10^{19} cm^{-3}) on an n-type (10^{15} cm^{-3}) Si substrate, viewed by means of the Everhart-Thornley type SE detector at 1 keV (left) and in the cathode lens mode with the primary beam energy 10 keV and landing energy 1 keV (right); width of the field of view 0.4 mm; reproduced from Ref. 13.

New experience was collected when observing the doped patterns in the cathode lens (CL) mode of an SEM [18]. First of all, the contrast was significantly larger than that acquired with a conventional SE detector of the Everhart-Thornley type (see Fig. 2), reaching a maximum around 1 keV of the landing energy [13]. The explanation was sought in the above-surface CL field that penetrates the junction structure and creates a space charge layer decreasing the n-type emission. Further, the contrast was established dependent on the surrounding vacuum environment in such a way that at "worse", i.e. less "dry" vacuum the contrast was higher. This finding motivated then the above mentioned experiments with metal coatings, and the concept of the sub-surface junction itself. These experiments also originated an idea about absorption of electrons once excited to above the vacuum level as another contrast controlling factor [13].

Altogether, the above-mentioned attempts to make the SE image signal the desired quantitative tool for examining the semiconductor structures have not been successful as regards ability to predict the image contrast reliably. Even newest data, presented elsewhere in this volume, provide more questions than answers. The way out might be sought in employing a simpler electron scattering mechanism producing the signal species of more closely defined properties.

One possibility is the electron backscattering at energies so low that release of SE could be neglected. The study [17] has been performed in a CL equipped UHV SEM (the Scanning Low Energy Electron Microscope, SLEEM) [18] by using the structure shown in Fig. 2. First of all, a contrast reversal was confirmed at energies below about 30 eV. This effect was expected as a consequence of the low energy electron reflectivity being inversely proportional to the local density of states coupled to the incident electron wave [19,20]. The observation is explained via penetration of incident electrons into empty dopant states above the vacuum level, which decreases reflection from the (p-type) doped patterns and hence reverses the contrast. More interesting and promising was, however, an extremely strong contrast observed

below about 3 eV, which was even capable of changing its sign in dependence of detection conditions (Fig. 3). The effect was found of a dynamic character, i.e. requiring the electron dose above a certain threshold and exhibiting a time constant in the order of seconds. Explanation is based on a conception of the p-type doped area to be negatively charged to about 1 V with respect to the surrounding substrate, which is enough to make the incident electrons totally reflected in a narrow "signal beam". This pencil can either escape the detection through the central detector bore or impact against the active detecting surface (Fig. 3). The proper phenomenon is then described as dynamic filling the conduction band to an extent sufficient for recombination of the majority holes, which leaves the ionized acceptors unbalanced [17]. This immobile negative space charge is then responsible for the mirroring. Possible quantifiability of this contrast type needs further examination.

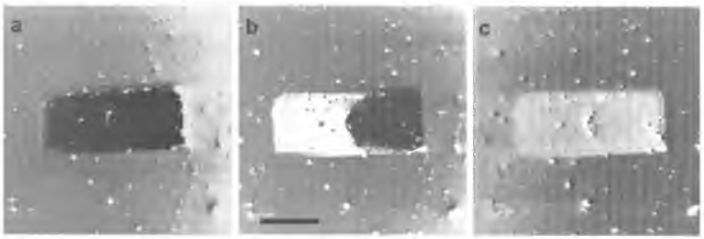

Figure 3: P-type patterns (10^{19} cm^{-3}) on an n-type (10^{15} cm^{-3}) Si substrate in the CL mode at 1.5 eV, specimen tilt 0° (a), 0.45° (b), and 0.72° (c); scale bar 20 μm, reproduced from Ref. 17.

Another alternative of how to avoid problems with the SE images is to excite the low energy electron signal with photons instead of electrons. Preliminary PEEM study of doped Si wafers [21] brought several surprising results. Although the energy unfiltered photoemission, excited with the Hg lamp radiation, gives again the p-type areas brighter, if only fastest photoelectrons are acquired, the image contrast inverts in both p/n and n/p patterned structures (Fig. 4). Further, the mutual shift between photoemission spectra from p- and n-type sites reaches only 0.12 to 0.14 eV (Fig. 5) and always the photo-threshold is larger for the p-type. Crucial is obviously the difference in amplitudes of the spectra. These findings clearly indicate not the ionization energy or surface barrier or near surface electric fields being responsible for the phenomena observed, but simply absorption of hot electrons on their trajectory toward surface. The main scattering mechanism is likely the e-h pair generation.

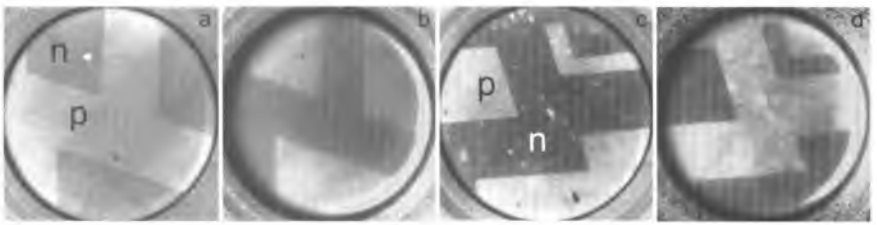

Figure 4: Photoemission micrographs of the p/n and n/p structures (both 10^{19} cm^{-3}/10^{15} cm^{-3}) taken in the total photoemission (a,c) and filtered with the threshold -0.36 V (see Fig. 5) (b,d).

Experimental as well as theoretical works in imaging the doped patterns in semiconductors are, and probably will be continuing although it seems at present that industrial applicators have lost their hope in getting the desired quantitative tool for the dopant profiling, and aim at managing with the CD measurements only. However, for the academic science the topic keeps to be attractive and promising adventures of cognition. [22]

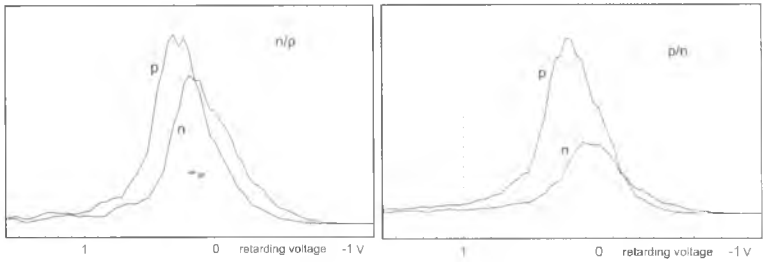

Figure 5: Photoemission spectra from the structures shown in Fig. 4.

[1] D. Venables, D.M. Maher, J. Vac. Sci. Technol. B 14 (1996) 421.
[2] D. Venables, H. Jain, D.C. Collins, J. Vac. Sci. Technol. B 16 (1998) 362.
[3] D.D. Perovic et al, Ultramicroscopy 58 (1995) 104.
[4] A. Howie, J. Microsc. 180 (1995) 192.
[5] A. Howie, in: Proc. 12th Eur. Congr. El. Microsc., Brno 2000, Vol. 3, 519.
[6] C.P. Sealy, M.R. Castell, P.R. Wilshaw, J. Electron Microsc. 49 (2000) 311.
[7] M.R. Castell, D.D. Perovic, H. Lafontaine, Ultramicroscopy 69 (1997) 279.
[8] S.L. Elliott, R.F. Broom, C.J. Humphreys, J. Appl. Phys. 91 (2002) 9116.
[9] M.M. El-Gomati, T.C.R. Wells, L. Frank, I. Müllerová, in: Proc. 12th Eur. Congr. El. Microsc., Brno 2000, Vol. 2, 635.
[10] M.M. El-Gomati, T.C.R. Wells, Appl. Phys. Letters 79 (2001) 2931.
[11] M.M. El-Gomati, T.C.R. Wells, I. Müllerová, L. Frank, H. Jayacody, IEEE Trans. Electron Devices 51 (2004) 288.
[12] M. El-Gomati, F. Zaggout, H. Jayacody, S. Tear, K. Wilson, Surface and Interface Anal. 37 (2005) 901.
[13] I. Müllerová, M.M. El-Gomati, L. Frank, Ultramicroscopy 93 (2002) 223.
[14] C. Schönjahn, R.F. Broom, C.J. Humphreys, A. Howie, S.A.M. Mentink, Appl. Phys. Lett. 83 (2003) 293.
[15] F. Mika, L. Frank, in: 9th Recent Trends, Brno 2004, 51.
[16] F. Mika, L. Frank, in: PDS 2004, ISI ASCR Brno, 37 (in Czech).
[17] L. Frank, I. Müllerová, Ultramicroscopy 106 (2005) 28.
[18] I. Müllerová, L. Frank, in: Advances in Imaging and Electron Physics 128 (2003) 309.
[19] R.C. Jaklevic, L.C. Davis, Phys. Rev. B 26 (1982) 5391.
[20] E. Bauer, Repts Progr. Phys. 57 (1994) 895.
[21] L. Frank et al., in: Proc. Microscopy Conf., Davos 2005, PSI Proceedings 05-01, 321.
[22] Study supported with the Czech Science Foundation under grant no. 202/04/0281.

POLY [METHYL (PHENYL) SILYLENE] LED DIODES - AS SEEN BY CATHODOLUMINESCENCE STUDY

P. Horák, P. Schauer

Institute of Scientific Instruments AS CR, Brno, Czech Republic, horak@isibrno.cz

Organic light emitting diodes (LEDs) have attracted much interest because of their potential for an efficient emission in visible region and for application to large area flat displays. LEDs utilizing conducting polymers have many advantages in terms of simple fabrication process of a thin film such as spin-coating or casting methods [1].

Polysilylenes (PSi) are linear silicon (Si) based organic materials whose basic building block is a chain built up of Si substituted by alkyl or aryl groups [2]. PSi are quasi one dimensional materials with delocalized σ-conjugated electrons along the polymer backbone chain. Their optical and electrical properties are primary ascribable to the effect of quantum confinement on these σ-conjugated electrons. PSi exhibit a sharp photoluminescence (PL) with a high quantum efficiency in solid state. The use of PSi in LEDs is attractive since this can emit light in the range from the ultraviolet to the visible regions [3]. But problems of life of PSi LEDs are discussed only in very few papers.

Organic LEDs generally show a degradation of their characteristics with time, such as increase of the threshold voltage and decrease of the fluorescence yield [4]. However, such an evolution depends on the polymer bulk modification and changes of the injection mechanism at the polymer-electrode interface. Cathodoluminescence (CL) is an interesting tool to study the polymer behaviour since it eliminates the injection problems.

Poly[methyl(phenyl)silylene] (PMPSi) is a typical representative of PSi. The absorption spectrum of PMPSi consists of three bands (Fig. 1) [5]. The electronic transition at 338 nm arises from delocalised σ-σ* transition. The PL spectrum of PMPSi consists of two emission bands – a sharp UV band at about 358 nm and a broad band in the visible part of the spectrum (Fig. 1). The sharp UV σ*-σ band is of exciton nature. The exciton is localized in the Si backbone. PMPSi was selected for our CL study. The PSi specimen preparation and CL method of the study were described previously [6].

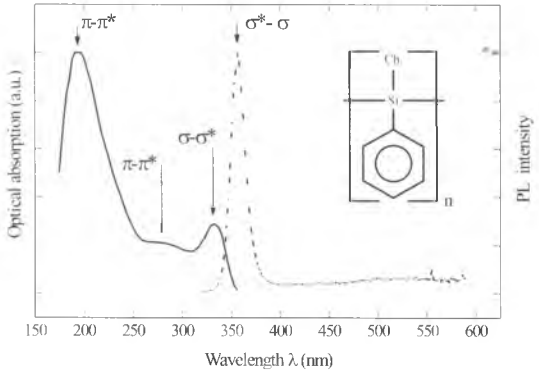

Fig. 1. Optical absorption (solid lines) and photoluminescence (PL) spectra (dash line) of PMPSi thin film [5]. The excitation wavelength for PL was set to 280 nm. Chemical structure of PMPSi is inset.

The decrease of the CL intensity of PMPSi at the different current densities of electron beam using the excitation energy of 10 keV is shown in Fig. 2. The curves have multi-exponential character. The decrease of CL intensity was assigned to a material degradation. The degree of polymer degradation is higher at the higher current density. After five minutes from the beginning of the excitation at the highest current density the decrease of CL intensity is as low as 40 % comparing with the beginning.

The CL spectrum of PMPSi (Fig. 3) is in good agreement with the PL spectrum of the same material (Fig. 1). The UV emission decreases rapidly with time, whereas the visible one remains nearly stable during electron beam irradiation. UV σ^*-σ deexcitation is related with the Si backbone (Si-Si bonds). Thus, the decrease of the CL intensity is a consequence of a Si-Si bond deformation. The Si-Si bond scission, crosslinking or the weakened bond formation is possible depending on conditions of excitation.

The fast decrease of the CL intensity with time impedes the utilization of pure PMPSi as an emissive layer in LEDs due to its short life. Doping of PMPSi with various stabilizers or absorbers can enhance material stability. According to the CL study, PMPSi with the susceptibility to electron beam degradation seems to be applicable as a resist in electron beam lithography.

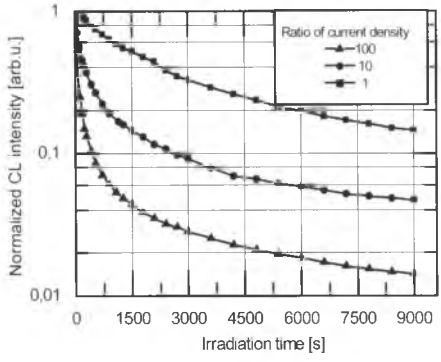

Fig. 2. The time decrease of the PMPSi CL intensity during electron beam irradiation at different current and the energy of 10 keV.

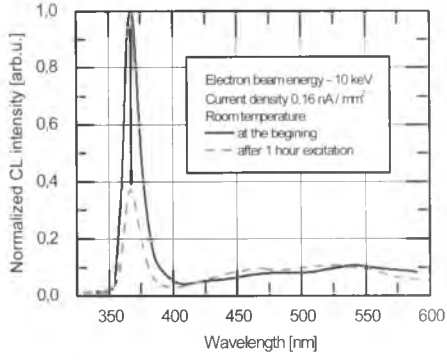

Fig. 3. Evaluation of the CL spectrum of PMPSi at the beginning and after 1 hour of electron beam irradiation.

References

[1] Fujii A., Yoshida M., Yoshimoto K., Ohmori Y., Yoshino K., Ueno H., Kakimoto M., Kojima H., Synthetic Metals 85 (1997) 1261-1262.

[2] Miller R.D., Michl J.: Chem. Rev. 89 (1989), 1359-1410.

[3] Fujii A., Yoshimoto K., Yoshida M., Ohmori Y., Yoshino K., Ueno H., Kakimoto M., Kojima H., Japan. J. of App. Phys. 35 (1996) 3914-3917.

[4] Davenas J., Boiteux G., Seytre G., Jardin C., Synthetic Metals 115 (2000) 83-87.

[5] Nespurek S., Journal of Non-Crystalline Solids 299 (2002) 1033-1041.

[6] Horak P., Schauer P., Proc. of 9th Inter. Seminar on Recent Trends in Charged Particle Optics and Surface Physics Instrumentation, Skalsky Dvur (2004), 31-32.

THE HIGH-PASS ENERGY FILTERED PEEM IMAGING OF DOPANTS IN SILICON

M. Hovorka[a,*], L. Frank[a], D. Valdaitsev[b], S. A. Nepijko[b], H. J. Elmers[b], G. Schönhense[b]

[a]Institute of Scientific Instruments, AS CR, Brno, Czech Republic
[b]Institute of Physics, Johannes Gutenberg University, Mainz, Germany
*e-mail address: hovorka@isibrno.cz

In the previous PEEM study [1, 2], focused on the origin of contrast between differently doped areas in silicon imaged by slow electrons, strong contrast was observed between p-type and n-type areas with the p-type brighter. The crucial mechanism was identified in electron absorption phenomena that are relatively weaker with emission from the p-type Si. The energy-filtered images of p- and n-type areas revealed differences in the energy distributions of photoemission. For the filter adjusted so that only the fastest electrons can pass to the detector, the contrast inverts and the n-type became brighter than p-type. The shift between p- and n-type photoemission spectra indicated larger photoemission threshold for the p-type.

Continuation of the study has produced results presented here. The photoemission spectra and micrographs for two sets of samples, n-type areas on a p-type substrate as specimens A and p-type areas on a n-type substrate as specimens B - both with different dopant concentrations varying from 10^{16} to 10^{19} cm^{-3}, are shown (Fig. 1 - 3). Si (100) wafers were prepared by standard procedures [1] and left in-situ uncleaned, i.e. with surfaces covered by a few nm layer of the native oxide. The samples were irradiated by UV light from the Hg lamp with a line at 4.9 eV and additional radiation between 3.2 and 4.4 eV.

The contrast inversion and corresponding shift between the p- and n-type spectra is present for all concentrations of dopants. While in the total-current photoemission image the contrast between p- and n-type area disappears when decreasing the dopant concentration, the inverted contrast behind appropriate threshold at the energy filter keeps to be distinctive. In the former image the surface relief is evident but in the fast-electron image the topographic contrast is suppressed which could indicate the electron signal acquired from larger depths (Fig. 2, 3).

The energy spectra exhibit some structure, possibly connected with multiple sources of photoelectrons (regular energy bands, bands of surface states). The difference in photoemission thresholds between p- and n-type increases up to 0.2 eV at highest concentrations (Fig. 1). For the specimen B the PEEM spectra also showed the photoemission yield increasing with the increasing p-doping level [3-5]. Furthermore, some changes have been detected in emissivity of surfaces exposed to prolonged UV light illumination (particularly with the specimen A).

References

[1] Frank L. *et al.*: Origin of the contrast in imaging of doped areas in silicon by slow electrons – to be published.
[2] Frank L. *et al.*, Proceedings of the 6th Dreiländertagung Microscopy Conference (2005).
[3] Allen F. G. and Gobeli G.W., Phys. Rev. **127**(1), 150-158 (1962).
[4] Ballarotto V. W., Siegrist K., Phaneuf R. J., Williams E. D., Mogren S., Surf. Sci. **461,** L570-L574 (2000).

[5] Ballarotto V. W., Siegrist K., Phaneuf R. J. and Williams E. D., J. Appl. Phys. **91**(1), 469-475 (2002).

[6] The study is supported by the Grant Agency of CR under grant no. 102/05/2327.

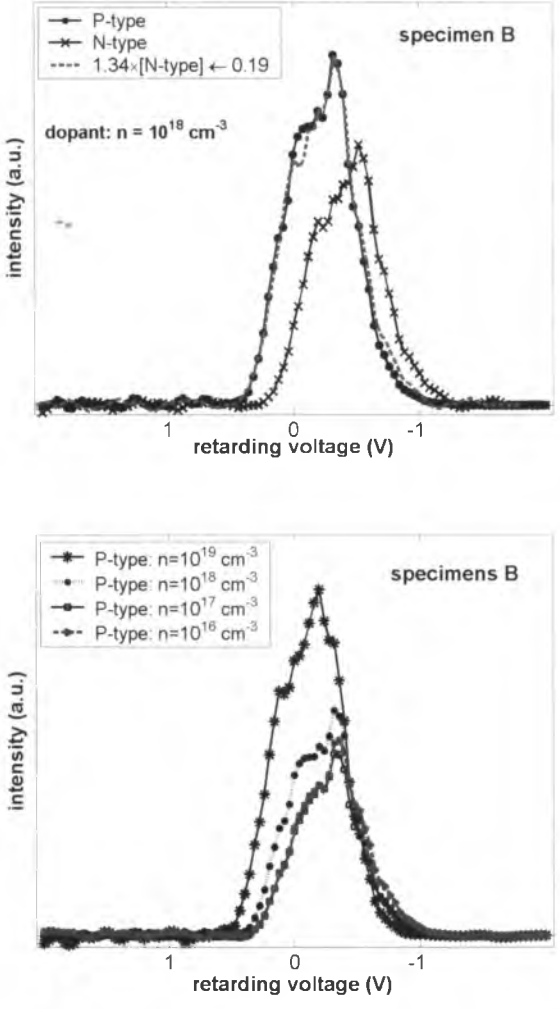

Fig. 1: Energy spectra of average photoemission signals from the p-type and n-type areas on the specimens B (p-type doped patterns on the n-type substrate of 10^{15} cm^{-3} carrier concentration). Top: data for the dopant density of 10^{18} cm^{-3}; dashed curve: the n-type spectrum normalized to fit the height of the p-type one, and shifted in order to coincide on the low energy side. Bottom: comparison of the p-type spectra for different dopant concentrations (top to bottom: 10^{19} to 10^{16} cm^{-3}).

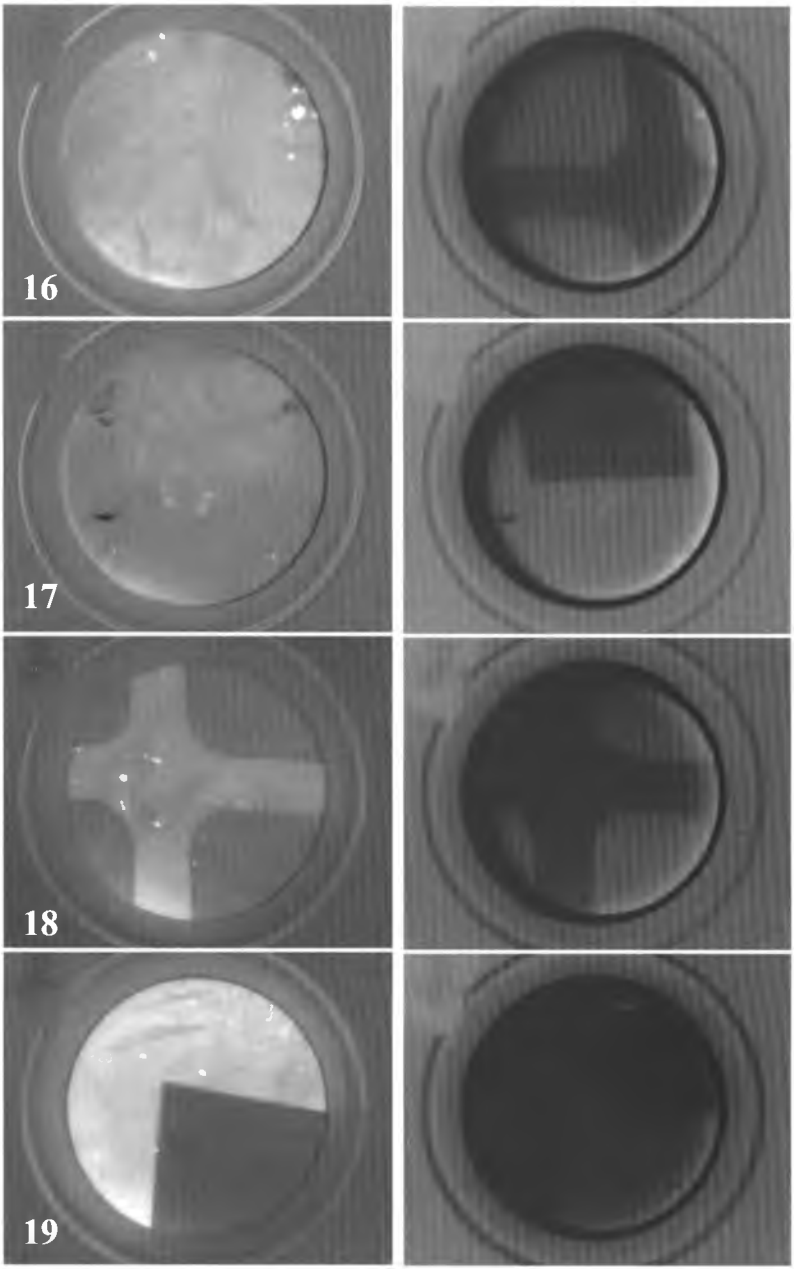

Fig. 2: PEEM images of the specimens B (p-type doped patterns on the 10^{15} cm^{-3} n-type substrate) with various dopant concentrations (top to bottom: 10^{16} to 10^{19} cm^{-3}). Left column: full photoelectron emission, filter bias of +1.64 V. Right column: filter bias of -0.44 V.

DIRECT RAY TRACING OF ELECTRONS THROUGH CURVED MAGNETIC SECTOR PLATES

Hung Quang Hoang, Junli Wu, Mans, Anjam Khursheed

National University of Singapore,
4 Engineering Drive 3, Singapore 117576.
E-mail: eleka@nus.edu.sg Tel. +6565162295.

Accurate ray tracing of electron trajectory paths through curved magnetic sector plates is required for a variety of different instruments, such as dispersion free beam separators [1] or energy spectrometer designs [2]. Since magnetic sector field distributions are inherently three-dimensional in nature, and often involve curved boundaries, direct ray tracing of electrons through them is a non-trivial task. Numerical field solving techniques such as the finite element method do not in general provide enough accuracy to extract aberration coefficients from the trajectory paths of focused beams in three dimensions. This is because numerical meshes in three dimensions that model complex shaped boundaries typically need over a million free nodes, requiring prohibitively large amounts of computer memory and unmanageably long program run times. The situation is made even more difficult for retarding sector units, where an electric field is overlaid onto the deflecting magnetic field in order to slow down electrons to very low energies (a few eV). Another disadvantage of using a fully finite element approach is that high-order interpolation methods are needed to extract accurate field information from nodal potentials. While not impossible to carry out, it is quite a challenge on curved mesh geometries in three dimensions, and therefore, mesh-less methods are preferred. In this paper, a semi-analytical approach is taken, one which uses a modified two-dimensional finite element solution in combination with a Fourier Series expansion. This approach avoids the direct use of a fully three-dimensional finite element solution, and has the desirable feature of not requiring a mesh in the region where electron trajectories are to be plot.

A two dimensional finite-element solution capable of modeling curved boundaries is first performed in the plane of the sector plates (x-y plane), as illustrated in Fig. 1. In this example, circular sector plates have an inner sector plate, an outer sector plate, and an outer round casing. The outer sector plate is set to unity potential, while the inner sector and casing is set to zero potential. Fig. 1a shows the numerical mesh, Fig. 1b shows the initial finite element solution, and Fig. 1c shows a modified finite element solution where central nodal coefficient P_0 is adjusted by a factor of $(1 + h^2/2d^2)$, where h is the mesh size in the x-y plane, and d is the distance to a zero potential odd-symmetry plane in the out-of-plane direction (z-direction). In this example, d = 1mm, and h = 0.25 mm. As expected, the influence of the zero-volt odd-symmetry plane causes equipotential lines to bunch towards the sector plate edges. A Fourier-Series expansion then integrates the potential in the plane of the boundary and calculates field values for any point inside the sector unit. This semi-analytical solution provides reasonably high accuracy when compared to the full three dimensional solution, which in this case, can be calculated accurately by a rotationally symmetric finite-element program, since the in-plane geometry is circular. Fig. 2 illustrates the accuracy of the semi-analytical approach for electric field values in the x-y plane 0.1 mm above the zero-potential odd-symmetry plane. The accuracy is plot as a function of the number of terms used in the Fourier-Series. The maximum electric field variation is divided by the maximum field strength value along a line running through the centre of the sector

unit. Fig. 2 shows that the percentage electric field error is smaller than 0.1 %. This approach is used to plot accurate direct ray paths through curved sector units, detailed examples of this will be presented.

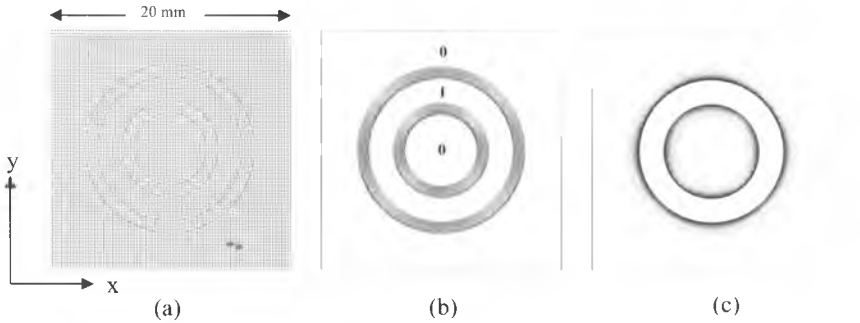

Figure 1: Finite-element solution in the plane of circular sector plates
(a) 81 by 81 mesh (b) 2D solution (c) Modified solution to account for nearby zero-potential symmetry boundary located 1mm away

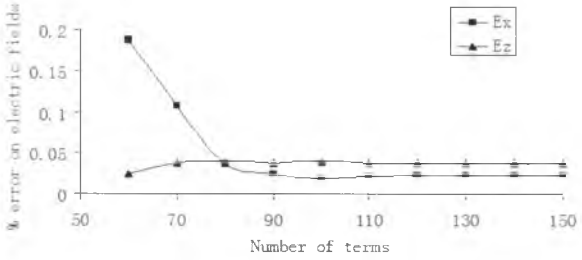

Figure 2: Accuracy of electric field values along the x-y plane for z = 0.1mm. Odd-symmetry boundary is at z = 0, distance to plane of plates is 1 mm

References

[1] H. Rose and D. Preikszas, *Optik*, 92, No. 1, 31-44 (1992).
[2] A. Khursheed and M. Osterberg, *Nucl. Instrum. and Meth. in Phys. Res* **A 556**, 437-444 (2006).

ATOM OPTICS VERSUS CHARGED PARTICLE OPTICS – A FUTURE CONTENDER?

Marcus Jacka, Andrew Pratt*

Email: marcus@hazelshaw.com
*Department of Physics, University of York, Heslington, York, YO10 5DD, United Kingdom

The manipulation of neutral atoms using resonant light gives rise to the possibility of novel forms of microscopy. We demonstrate the rudiments essential for achieving this, namely focussing and scanning, using metastable helium atoms as an example. In the second part of the paper we propose a novel form of ion microprobe, this time using resonance ionisation, which could overcome some of the disadvantages of conventional liquid metal focussed ion beams.

Introduction

The ease with which photons, electrons, and ions can be focussed and otherwise manipulated is reflected in the maturity of optical and charged particle microscopies. Sub-wavelength resolution can now be achieved with scanning near-field optical microscopy, whilst the use of aberration correctors has brought transmission electron microscopy to sub-Angstrom resolution. Neutral atoms, as their name implies, are much less susceptible to manipulation, however they have desirable properties in terms of surface analysis, microscopy and nanofabrication. At thermal energies, of tens of millivolts, there is negligible penetration of the atoms below the surface, meaning that the information area is confined to the size of the probe. Despite their low energy, the mass of atoms compared to electrons leads to small de Broglie wavelengths. Two other advantages of neutral atom beams must be mentioned. One is the lack of repulsive Coulomb forces between the particles and similarly the lack of screening which gives rise to the Boersch effect. The other is that because non-conservative (for example velocity dependent) forces can be applied to neutral atoms with laser-cooling techniques, the Helmholtz-Lagrange relation does not apply. As a result the energy normalised brightness ($Acm^{-2}sr^{-1}eV^{-1}$) of the microprobe at the sample is not limited to the brightness of the source.

Manipulation of neutral atoms

Laser cooling, or manipulation using light forces, is the newest, and also the most promising of a number of methods by which a beam of neutral atoms can be deflected, focussed or otherwise manipulated. The first methods were developed by Stern, Rabi and others in the 20s and 30s, making use of the force exerted by an inhomogeneous magnetic field on atoms with magnetic dipoles. Later it was shown that magnetic lenses could be created from hexapole magnetic fields. Combined with laser cooling to first collimate and reduce the longitudinal velocity distribution of the atom beam, spherical and chromatic aberrations can be significantly reduced [1]. Further techniques include the focussing of ground state helium atoms by specular reflection from clean silicon mirrors [2], and the use of Fresnel diffraction lenses [3].

Laser cooling encompasses a broad range of techniques, and since the mid-eighties it has become a rapidly expanding field in its own right - there are many excellent books and reviews (see eg [4], and references therein) to which the reader is directed. The simplest method makes use of the force (known as the spontaneous force) resulting from the momentum exchanged in the absorption/emission process between an atom and quasi-resonant photons. Because of the narrowness of atomic linewidths, both velocity dependent forces (due to the Doppler effect) and spatially dependent forces (by application of inhomogeneous magnetic fields) are possible. More sophisticated methods allow the precise positioning of single atoms and arrays of atom beams to within tens of nanometres [5].

At York an instrument has been constructed to crudely focus and scan a beam of metastable 2^3S helium atoms, to perform metastable de-excitation spectroscopy (MDS) [6]. Whilst this is not a microscope (the focussed beam has a diameter of ~2mm) it demonstrates some of the principles necessary for a microscope, and can be developed further in that direction.

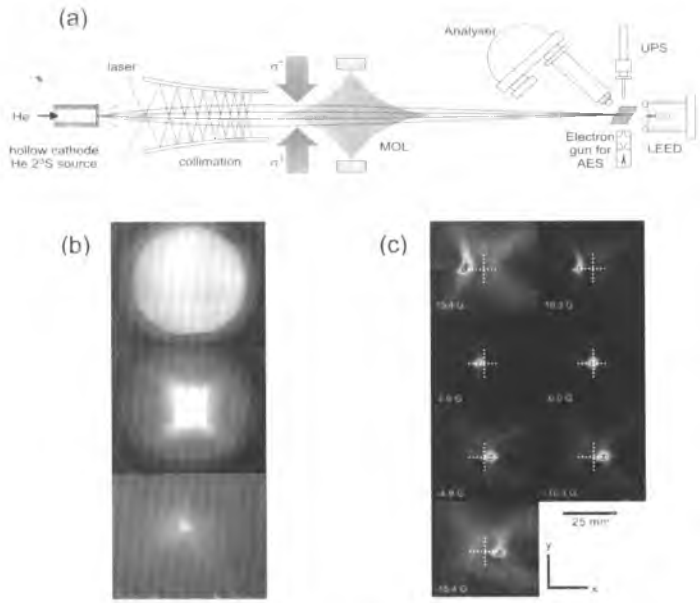

The York MDS instrument. (a) Schematic showing the main collimating, focussing and surface analysis components. (b) The beam profile before collimation (top), the collimated beam (middle), and the focussed beam (bottom). (c) Left-right scanning of the focussed beam using electromagnetic scan coils superimposed on the magneto-optic lens.

Resonance ionisation focussed ion microprobe

A further application of the narrow linewidth lasers of the sort used in the MDS instrument could be the creation of a high-brightness ion source. Effusive or supersonic neutral atom beams can easily be produced, are high density and have narrow energy distribution [7].

Ionisation can be performed efficiently and in a highly localised fashion with two intersecting focussed laser beams. One raises the atom from its ground state to an excited state, the second, possibly of the same wavelength, ionises the excited atom. The ions can then be extracted and focussed with a simple electrostatic lens. This process of resonance ionisation is well established in other fields, particularly mass spectroscopy, and schemes have been developed for every element except helium [8]. It is suggested that a resonance ionisation focussed ion microprobe would have spatial resolution equal to current liquid metal ion sources, be able to operate at significantly lower energy (the energy spread of an LMIS is approximately 3eV, so has to be operated at high energy to minimise chromatic aberrations) and could be developed for virtually any atomic species.

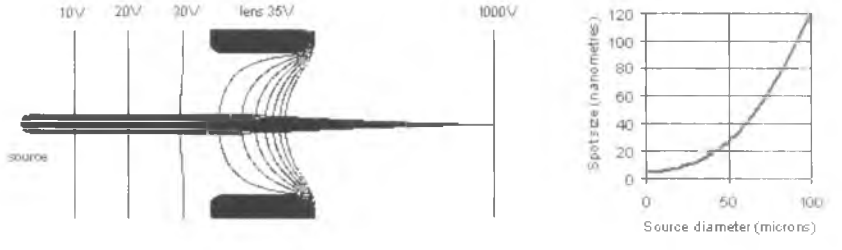

Modelling of ion trajectories for a resonance ionisation focused ion microprobe. It is predicted that a laser interaction volume of less that 25μm diameter would produce a focussed ion beam less than 10nm in diameter.

Conclusion

One of the encouraging aspects of this area of research is that current techniques for manipulating neutral atoms are very much in their infancy. In contrast, conventional charged particle optics is a mature subject, and advances are necessarily more incremental in nature. Its practitioners would do well to follow the progress of its younger rival.

References

[1] WG Kaenders, F Lison, A Richter, R Wynands, D Meschede, Nature **375**, 214 (1995)
[2] B Holst and W Allison, Nature Nature **390**, 244 (1997)
[3] O Carnal, M Sigel, T sleator H Takuma and J Mlynek, Phys. Rev. Lett. **67**, 3231 (1991)
[4] H Metcalf and P van der Straten: *Laser cooling and trapping*. Springer (1999)
[5] JJ McClelland, RE Scholten, EC Palm, and RJ Celotta, Science **262**, 877 (1993)
[6] A. Pratt, A. Roskoss, H. Menard and M. Jacka, Rev. Sci. Instrum. **76**, 053102 (2004).
[7] NF Ramsey: *Molecular beams*. Oxford University Press, (1956)
[8] GS Hurst and MG Payne: *Principles and applications of resonance ionisation spectroscopy*. Adam Hilger, (1988)

CALCULATIONS OF THERMIONIC ELECTRON GUN FOR MICROMACHINING

P. Jánský

Institute of Scientific Instruments ASCR, Královopolská 147, 612 64 Brno, Czech Republic
jansky@isibrno.cz

Kinetic energy of electrons incident on the surface is changing into the thermal energy. The beam with high current density can be used for melting or vaporizing materials and for modifications of the material surface. Beams with small diameters can be used for drilling very small holes and creating sieves. Magnetic deflection of the beam enables very high productivity of thousands holes per second.

The electron beam-welding machine [1] in ISI Brno is intended for joining components and materials used in electron optical instrumentation and vacuum engineering, but in the last years its capability was extended for experiments in micromachining [2]. As an electron source a thermionic cathode with tungsten hairpin filament is used. Typically the beam energy is 50 keV, the maximum power is about 1.5 kW. The optical part consists of four main parts (fig 1): electron gun, centering and stigmator coils, a magnetic lens and a deflection system.

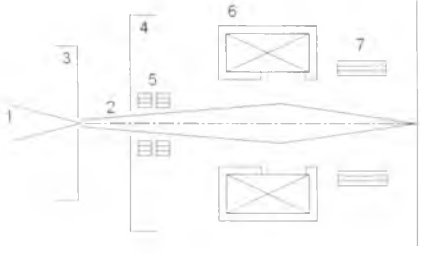

Fig. 1: Scheme of the optical system of the electron-beam welding machine: 1) cathode, 2) electron beam, 3) wehnelt electrode, 4) anode, 5) centring coils and stigmator, 6) magnetic focusing coil, 7) deflecting coils .

To achieve higher current densities and smaller beam diameters, we started with numerical simulations and optimizations of the electron-optical system. The beam properties depend mostly on the electron source, therefore we started with the simulations of the electron gun, where the space charge effect is significant [3].

For the simulations we use program EOD [4]. Field calculation is based on the finite element method. Space charge distribution is iteratively evaluated from the ray tracing. From the field intensity and potential distribution near the cathode surface a new value of the emission current limited by space charge is established. Then the space charge distribution is recalculated for the new emission current until this process converges. The electron gun is simulated as a rotationally symmetric problem. Emitting surface of the hairpin filament cathode is approximated by a blunted cone with a spherical cap. The shape of the cathode makes the left border of the mesh. In our simulation (fig. 2) we set the filament on 0 V and the anode is on 50 kV.

We are testing and improving our new algorithms for space charge limited thermionic emission and analyzing current electron gun [1]. In the next months we want start with the design of a new electron gun and focusing optics designed with respect to requirements of micromachining.

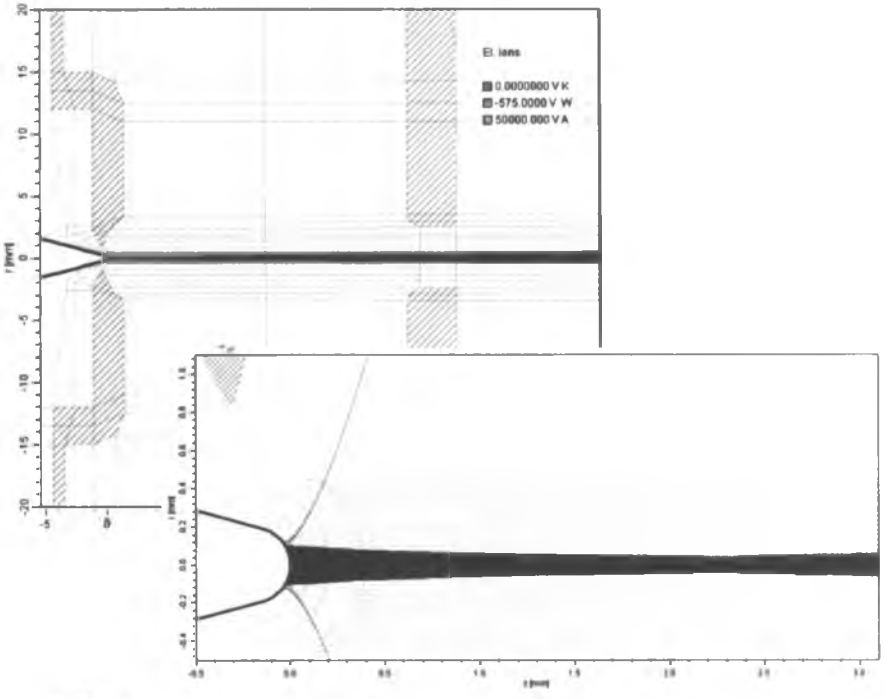

Fig. 2: Simulation of the thermionic electron gun in EOD. From the heated cathode approximated with a blunted cone with a spherical cap the electron beam is emitted.

[1] Dupák J., Vlček I., Zobač M.: Electron gun for computer-controlled welding of small components. Vacuum **62** (2001) 159-164.

[2] Dupák L., Dupák J., Zobač M.: Creation of fine holes into quartz by electron beam (in Czech). Jemná mechanika a optika (Fine Mechanics and Optics) **51**, 1 (2006) 10-12.

[3] Jánský P., Lencová B., Zlámal J.: Optimalizations of optics of an electron-beam welding machine (in Czech). Jemná mechanika a optika (Fine Mechanics and Optics) **50**, 2 (2005) 46-48.

[4] Lencová B. and Zlámal J.: New CAD program for the design in electron optics. Proc. EUREM 2000, Brno, Vol. I, 101-102.

SCINTILLATION SE DETECTOR FOR VARIABLE PRESSURE MICROSCOPES

J. Jirák[1,2], J. Linhart[1,2] and V. Neděla[1]

[1] Institute of Scientific Instruments AS CR, Královopolská 147, Brno, Czech Republic
[2] Faculty of Electrical Engineering and Communication, BUT, Údolní 53, Brno, Czech Republic
jirak@feec.vutbr.cz

Scintillation detectors are frequently used for the detection of secondary electrons in scanning electron microscopes. In order to achieve an efficient scintillation in these detectors, sufficient energy must be added to secondary electrons by an accelerating electrostatic field. This field is usually created by connecting a voltage of 10 kV to the thin conductive layer prepared on the surface of the scintillator. To add such a voltage to the scintillator of the detector may be a problem in the case when the detector with the scintillator is placed in a specimen chamber of a variable pressure microscope at a pressure of several hundreds Pa because of electric discharges in gas. In this case, the connection of a high voltage to the scintillator requires placing the scintillator in a separate room where the pressure does not exceed several Pa. Simultaneously, it is necessary to permit secondary electrons to travel from the specimen chamber to the room where the scintillator is located.

In case of the proposed detector, separation of the room with scintillator from the specimen chamber is accomplished by a system of two pressure limiting apertures with central openings diameters of several hundred μm and by a separate pumping of the rooms by a rotary pump and by a turbomolecular pump as is seen in Fig.1a. Owing to the vacuum system the pressure of several Pa can be maintained in the scintillator room while the pressure in the specimen chamber reaches 2000 Pa, Fig.1b.

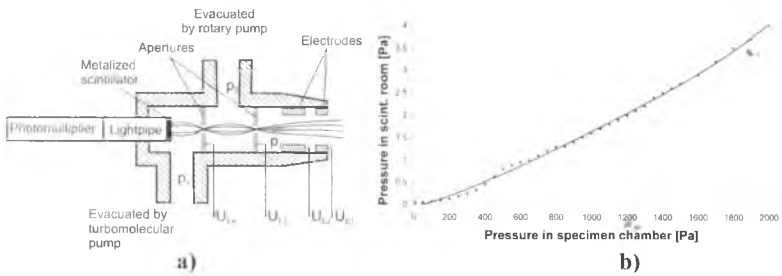

Fig.1. a) Schematic drawing of detector.
b) Dependence of pressure in scintillator room on pressure in specimen chamber.

A voltage of several hundred volts is connected to the pressure limiting apertures, and an electrostatic lens is created which together with voltages on other detector electrodes enables the secondary electrons to pass through from the specimen chamber to the scintillator room. In the scintillation room, the secondary electrons are accelerated by the electrostatic field with a voltage of 10 kV to the scintillator. Trajectories of secondary electrons simulated for one version of the detector electrode system are shown in Fig.2a. Trajectories were simulated by Simion Ver.7 program [1].

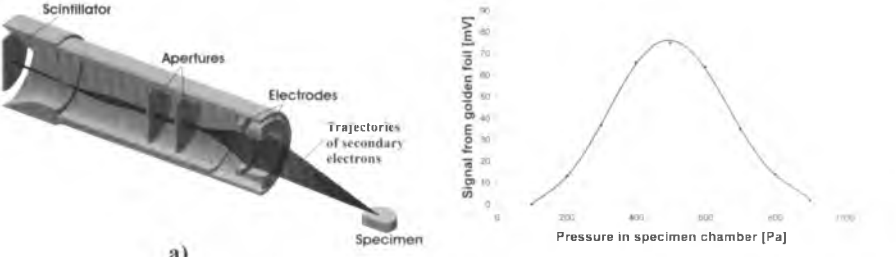

Fig.2.a) Trajectories of secondary electrons of 5 eV in detector electrostatic field. Voltages on electrodes U_{E1} = 2 V, U_{E2} = 10 V, U_{E3} = 500 V, U_{E4} = 750 V, voltage on scintillator 10 kV.
b) Measured dependence of detected signal from golden foil on pressure in specimen chamber. Voltages on electrodes U_{E1} = 10 V, U_{E2} = -8 V, U_{E3} = 450 V, U_{E4} = 750 V.

The dependencies of the signal detected from the golden foil on the pressure in the specimen chamber were measured for changing voltages on individual electrodes. One of the measured dependencies is shown in Fig.2b for voltages on electrodes U_{E1} = 10 V, U_{E2} = -8 V, U_{E3} = 450 V, U_{E4} = 750 V. Some results of observations of a gilded copper grid using this detector are in Fig.3. Introductory experiments with this detector confirm the possibility of its exploitation for observation of specimens up to a pressure of about 900 Pa in the specimen chamber.

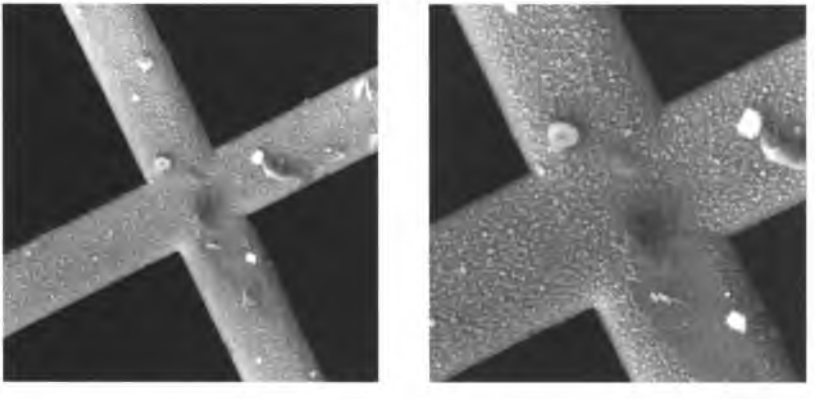

Fig.3. Observation of gilded copper grid by proposed detector at pressure 200 Pa, magnification a) 500 x, b) 1000 x.

[1] SIMION 3D Version 7.0 User's Manual, David A. Dahl, INEL-95/0403 rev. 5, 2000.
[2] This work was supported by project GAČR No. 102/05/0886 and by project MSM 0021630516.

SIMULATED PERFORMANCE OF A TIME-OF-FLIGHT ELECTRON EMISSION MICROSCOPE (TOFEEM)

Anjam Khursheed and Ding Yu

National University of Singapore, 4 Engineering Drive 3, Singapore 117576.
eleka@nus.edu.sg

Over the last four years, proposals for time-of-flight electron emission microscopes (TOFEEMs) have been made, both with and without methods to dynamically correct for chromatic aberration [1, 2, 3]. Correction of aberrations in time is an important alternative to the more widely discussed tetrode mirror method [4, 5]. This is because the tetrode mirror method has a relatively complicated column design, where its photoelectrons are designed to trace trajectory paths around a multiply curved axis, requiring the use of special alignment strategies for its beam separator [6]. The TOFEEM column in comparison, is relatively simple. Fig. 1 depicts the basic layout of a dynamic chromatic aberration corrected TOFEEM. Apart from the complication of pulsing the source irradiation with pulse widths in the sub-nanosecond range and modulating the potential on a lens electrode at a rate of several volts per nanosecond (indicated by $V_c(t)$ in Fig. 1), the TOFEEM has a single straight electron optical axis where photoelectrons are successively focused and magnified using standard projection principles.. The TOFEEM also has the added advantage of inherently being an energy spectrometer, which can readily band-pass filter the photoelectrons that make up the final image by simply capturing them over a series of different time windows. In the tetrode mirror method, an additional energy spectrometer must be used.

In this paper, the possible advantages of TOFEEM, both with and without dynamic chromatic aberration will be examined. In particular, the residual resolution, dominated by spherical aberration, will be estimated for two different objective lens designs, and presented in a form that can be compared with predictions already made for the conventional PEEM as well as the tetrode mirror form of aberration correction. Wan et al have predicted that the tetrode mirror method will be able to provide 4 nm resolution at 2% transmission, as opposed to 20 nm at 1% for conventional PEEMs [5]. In this work, it will be shown that TOFEEM is predicted to provide better image resolution than a conventional PEEM, and that dynamic correction of chromatic aberration through TOFEEM is expected to achieve a similar performance as that predicted for the tetrode mirror form of aberration correction.

References

[1] A. Khursheed, Optik 113, No. 11 (2002), p505-9
[2] G. Schonhense, A. Oelsner, O. Schmidt, G. H. Fecher, V. Mergel, O. Jagutzki, and H. Schmidt-Bocking, Surface Science 480, (2001), p180-7
[3] G. Schonhense, J. Vac. Sci. B 20(6), (2002), p2526-2534
[4] P. Hartel, D. Preikszas, R. Spehr, H. Muller, and H. Rose, Advances in Imaging and Electron Physics, **120**, pp. 41-132, (2002)
[5] Wan, J. Feng, H. A. Padmore and D. S. Robin, Nucl. Instrum. and Methods in Phys. Res. A, Vol. 519, Iss 1-2, (2004), 222-9
[6] P. Schmid, J. Feng, H. Padmore, D. Robin, H. Rose, R. Schlueter and W. Wan, Rev. Sci. Instrum. 76, 023302, (2005)

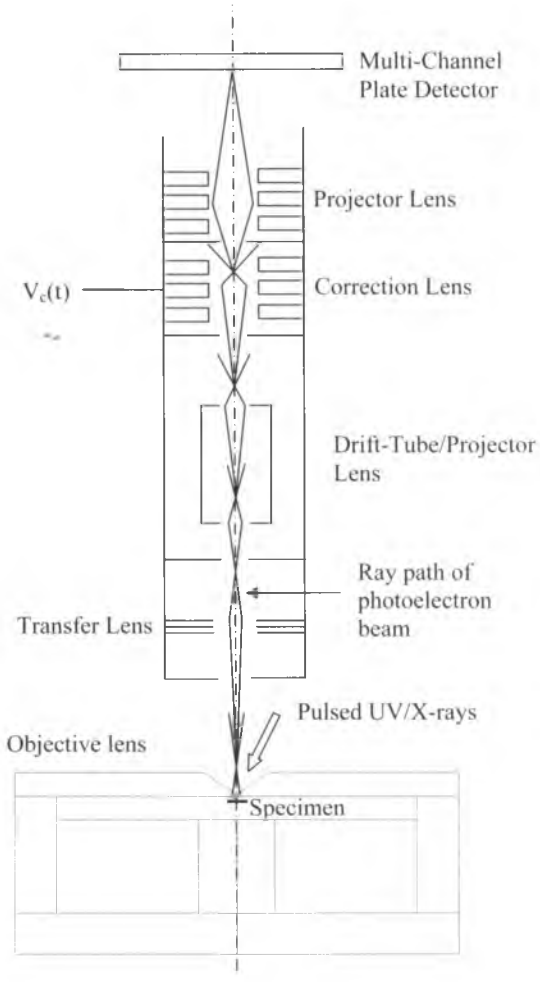

Figure 1: Schematic for a dynamic chromatic aberration corrected TOFEEM

PROGRAMS FOR ELECTRON OPTICAL DESIGN

B. Lencová, M. Oral

Institute of Scientific Instruments AS CR, Královopolská 147, 612 64 Brno, Czech Republic

1. Introduction

The computations in particle optics can be divided into "serious" ones, where the program packages provide a solution to a number of electron optical problems and express the final results in terms understood in electron optics like the aberration coefficients, and to approaches coming from outside of the electron optical community, which do not or cannot provide such answers. The basis of serious programs is an accurate computation of 2D electrostatic and magnetic focusing and deflection fields and programs/modules for the computation of optical properties from aberration theory or from accurate ray tracing [1-3].

Saturated magnetic electron lenses represent a very important class of problems, and the FEM is the only method which can analyze them (saturated lenses cannot be solved with CDM [4]). The advantage of CDM is, however, the ease with which electrostatic systems like FEGs with orders of magnitude difference in dimensions can be computed easily. Other problems like the deflection systems and their aberrations are not studied in 2D [5]. Computation of magnetic lenses with FDM/CDM is not very promising [6]. 3D computations in SIMION have reached quite an advanced level [7]; this was the first Windows program, although now it looks a bit old fashioned, and its biggest advantage is the low cost. When applied to electron optical problems, sometimes quite curiously looking results can be reached and the aberrations are not easy to dig out [8].

Electron optical design is done nowadays by commercial firms, so hardly any interesting lens geometries are found in recent literature. What is also difficult to find are accuracy and test cases or benchmarks, the only exception being an attempt in [9] which concentrated on electrostatic problems suited rather to CPO programs. Nowadays, more and more complex problems can be and are being solved. From the user point of view it is important to have simple but accurate and easy to use tools for the computation working under Windows XP. The software is not intended to people without some preliminary knowledge of electron optics, although quite often it is possible to meet a large degree of ignorance.

In this paper, attention will be given first to questions of accuracy of FOFEM as an example of computation method, followed by a discussion of the requirement of accuracy for the evaluation of optical parameters. Finally interesting recent result will be shown.

2. The FOFEM

Before starting a brief overview of the accuracy of FOFEM, let us briefly mention the user aspect of our software. The older 2D FOFEM packages were replaced with a new EOD program, in which we can analyze quite complex systems with many elements, lenses, deflectors and multipoles. Optimization procedures are used to adjust the image position, in particular with the accurate ray tracing, and space charge module allows the computation of intensive electron and ion sources, as discussed separately in these proceedings. Even if we want to improve the input and output of ray tracing, extraction of aberration coefficients from ray tracing results, and analysis of spot profiles and emittance diagrams, in its current form the program is stable, user friendly and easy to use, tested by a number of users as well as on

undergraduate and postgraduate students. The computation speed is nowadays so high that it makes no sense whatsoever to perform the field computation in meshes with less than say 50000 mesh points, so most of previous discussions about FEM computations as reflected in [10] have become irrelevant. In FEM as used in electron optics [3], using the topologically regular meshes, the biggest problem is the requirement for the correct generation of the coarse and fine mesh. The simple topology of the mesh makes the computation faster and easier compared to standard FEM with triangles, but also sometimes more difficult to comprehend. There are still some persistent myths that will be briefly mentioned.

Electrostatic lenses

In the past it was claimed that electrostatic lens cannot be computed with FOFEM and rays can never be traced through such fields because on axis FOFEM is inaccurate. In a square mesh the FOFEM provides on axis for a central point the difference equation $(V_{left}+V_{right}+3*V_{top})/5$ whereas the 5-point FDM gives a better and correct value $(V_{left}+V_{right}+4*V_{top})/6$, where the potential at both axial points and nearest off-axis point is involved – and this claim was repeated even quite recently [11]. This is not true, after a small correction the FOFEM equations on axis in rectangular meshes are the same [12]. FOFEM accuracy has been successfully tested both for a fields and tracing in [9]. Moreover, in EOD our practical procedure is used to point to user errors in meshing [13]. In short, the former problems with FOFEM can rather be assigned to the use of low number of mesh points or user errors in generating the coarse or fine mesh for the computation.

For example, when Liu [14] analyzed "typical" electrostatic lenses, for a two-tube lens (gap 0.1D, object at -3D and image at 3.93D for 8x acceleration, see figure 1 in [15]), he had the potential computed with 400x20 mesh points with FDM. For the computation of optical properties he needs 1600 points on axis, but for the larger mesh with 1601x81 points he would need just in 3 s on 3 GHz PC with FEM! His axial potential is computed with field error on axis of 0.025% compared to the correct results of another Chinese scientist, Yan, tabulated by Liu in [14].

Magnetic lenses

It was discussed extensively in the past that vector potential in FOFEM never provides correct results for specific problems in small meshes [10]. Even in this case we have suggested a solution in FOFEM, namely to use flux instead of vector potential and to perform a proper integration. The new formulas are not too much more complicated than the previous ones, but they work on all the previously reported "pitfalls". Again, the accuracy of the results can be checked with a simple procedure used in mesh methods in mathematics [16]. The error is easy to understand for axial flux density but it is also available at off-axis point even for highly saturated objective lenses with complex geometry, demonstrating that the axial flux density can be computed to an accuracy of 0.01%. The actual source of errors is then only the user by defining wrong coarse mesh, wrong position of the border and wrong boundary condition, wrong fine mesh with too few fine mesh lines, wrong magnetization curves, and by not checking even the most trivial result showing the validity of Ampere law. No benchmark tests are available for magnetic lenses.

Deflectors and multipoles

By computing the reduced scalar potential Φ_m/r^m instead of Φ_m and by performing proper integration of FOFEM coefficients (including the correction on axis as in scalar potential), accurate axial field can be obtained for the lowest three harmonics of magnetic deflectors in

air, which can be compared with analytical expressions even for tapered coils [17]. EOD computes the axial multipole function up to m=8. No accuracy tests are available as well, except for misleading information that only SOFEM provides the hexapole and decapole field function for deflectors [3]. For multipole systems the exact shape of the field is actually less critical (quadrupole systems are often sufficiently characterized with SCOFF, even deflection aberrations do not strongly depend on the accurate shape of the deflection field [18]).

3. The optical properties

What accuracy of computation we need? With what accuracy do we need to know the position of the focus, the value of the axial aberration coefficient of the third and fifth order? We have stated that for the fields on axis the accuracy can be very high, below 0.01% (actually in the past a much stronger requirement was that the field is smooth so that it can be correctly interpolated). As a matter of fact, the focal distances and aberrations (3^{rd} order geometrical and 1^{st} order chromatic) can be computed often with the same or better accuracy than the field by solving the paraxial trajectory equation and by computing aberration integrals.

The low number of mesh points was actually the main reason why tracing could not be done properly or easily, the 2D data are more difficult to interpolate than 1D axial result, and so they may produce uncontrollable local errors. The error estimate brings information about possible mesh errors [13, 16]. However, it is not so trivial to get the aberrations from the direct ray tracing by solving the equation of motion, otherwise one of the first published attempts to get aberrations of a simple dipole mirror would not fail [3, 19]. Unfortunately Liu [14], who analyzed "typical" electrostatic lenses to up to 5^{th} order geometrical aberrations with his own aberration formulas and with DA program, used just very weak electrostatic lenses, which are not a proper example to check our results against his results.

4. Aberrations from ray tracing and spot profiles

One of the difficult tasks is also the evaluation of spot profiles. For such a purpose, in order to get smooth representative curves, it is desirable to know the positions of a very large number of particles, say a few billions, in a given observation plane. We can then take into account the spot profile in the object plane, the energy width of the beam, the aperture position and diameter. The best procedure we use for this purpose is to get from a representative set of particles, say a thousand or so, computed by accurate ray tracing, the aberration coefficients of any required type and order [20]. The coefficients are obtained by regression, so that the quality of the fit is easily estimated.

As an example of a difficult system to analyze we show here the preliminary results of computations of probe profiles of a very low voltage scanning electron microscope. The system consists of an electrostatic lens followed by a cathode lens, slowing down the beam of 5 keV electrons to just 1 eV energy. The figure at the left shows the beam profile after this system in the Gaussian image plane, demonstrating a good resolution of such an arrangement, even if the beam energy width is also 1 eV. After we switch the Wien filter on [21] (the filter is placed in the crossover above the lens, it acts as a weak electrostatic lens and an energy dispersion element. Without changing the lens settings, the beam size becomes larger, but 10 micrometers towards the lens the beam shape changes, making the spot size smaller and astigmatic (see Figure 1).

5. The future

EOD is a modular program and it makes a good basis for further improvements. We hope to present more computation of difficult problems in electron optics such as mirror and

multipole correctors and evaluation of higher order aberrations. In the future we plan to add into EOD the analysis of dynamic corrections of aberrations of high accuracy deflection systems, the analysis of misaligned systems, and eventually stochastic Coulomb interactions.

Acknowledgement: Supported by the Institutional Research Plan AV0Z20650511 of AS CR.

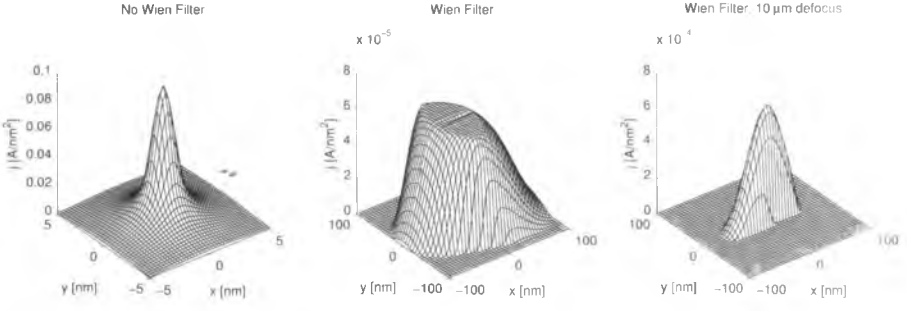

Figure 1. Current density in the Gaussian image plane of a LV SEM at 1 eV average beam energy. On the left hand side is the beam profile behind the electrostatic and cathode lenses, in the central figure after the Wien filter is switched on, and the profile on the right holds for 10 micrometers above the image plane.

References:

[1] B. Lencová, Proc. Recent trends (9th seminar), Brno 2004, 43-46.
[2] A. Khursheed, The finite element method in charged particle optics. Kluwer, 1999.
[3] J. Orloff, ed. Handbook of Charged Particle Optics. CRC Press, Boca Raton, 1997.
[4] B. Lencová, Nucl. Instr. Meth. in Phys. Res. **A 519** (2004), 133.
[5] http://www.eleetronoptics.com
[6] R. Becker, G. Martinez, A. v.d.Weth, Nucl. Instr. Meth. in Phys. Res. **A 519** (2004), 49.
[7] D.A. Dahl, SIMION 3D VERSION 7.0, User's Manual, 1995.
[8] O. Sise, M. Ulu, M. Dogan, Nucl. Instr. Meth. in Phys. Res. **A 554** (2005), 114.
[9] D. Cubric, B. Lencová, F. H. Read, J. Zlámal, Nucl. Instr. Meth. in Phys. Res. **A 427** (1999), 357.
[10] B. Lencová, Nucl. Instr. Meth. in Phys. Res. **A 427** (1999), 329
[11] E. Kasper, Adv. Imag. Eleetron Phys. **116** (2001).
[12] B. Lencová, M. Lenc, Scanning Electron Microscopy 86, Part III (1986), 897.
[13] B. Lencová, M. Lenc, Nucl. Instr. Meth. in Phys. Res. **A 519** (2004), 141.
[14] Z. Liu, Ultram. **106** (2006), 220.
[15] B. Lencová, Proc. Recent trends (10th seminar), Brno 2006.
[16] B. Lencová, Nucl. Instr. Meth. in Phys. Res. **A 519** (2004), 149.
[17] M. Lenc, B. Lencová, Review of Scientific Instruments **68** (1997), 4409.
[18] M. Lenc, B. Lencová, Optik **78** (1988), 127.
[19] B. Lencová, Proc. Recent trends (5th seminar), Brno 1996, 55.
[20] M. Oral, PhD Thesis, Brno 2006 (to be published).
[21] I. Vlček, B. Lencová, M. Horáček, Proc. MC2005, Davos, 59.

EOD (ELECTRON OPTICAL DESIGN) PROGRAM FEATURES

B. Lencová[a,b] and J. Zlámal[b]

[a] Institute of Scientific Instruments AS CR, Královopolská 147, 612 64 Brno, Czech Republic
[b] Institute of Physical Engineering, Faculty of Mechanical Engineering, Brno University of Technology, Technická 2, 619 69 Brno, Czech Republic

From the point of view of a user of electron optical programs for the design in microscopy it is important to have simple and easy to use tools for the computation. Standard for most CAD programs is that they work under Windows XP, use a mouse, on-line help, and provide simple guidelines and examples for working with them.

Based on 15 years of experience with 2D FOFEM packages that were developed in the course of many years, partly at ISI Brno and TU Delft, and that were equipped with a graphical input and display interfaces in DOS [1], we considered that the whole system has to be transferred into Windows. The first but only a preliminary version we showed in 2000 at EUREM in Brno [2]. All FEM programs for lenses and deflectors were integrated in a single program, their interfaces were programmed, and the modules for the computation of optical properties and ray tracing have been written completely from scratch in order to introduce a number of improvements in comparison to the old software. EOD is a modular program, compiled in Visual Fortran, allowing programming of all Windows graphics; use a mouse, pull-down menus, dialog windows, and on-line Help (see Figure 1). EOD uses a clearly defined project structure to analyze complex systems with many elements, lenses, deflectors and multipoles. Optimization procedures allow that the excitations are adjusted to achieve given image position, spot size or similar. Space charge module allows the computation of intensive electron and ion sources [3].

Field computation by the first order FEM is no more a critical issue; by using a large number of points (one minute computation is needed for around 700000 point meshes on 3 GHz P4 PC), error of field can be quite small and it can be simply identified and estimated. The size of the coarse and fine meshes for FEM is virtually unlimited because of dynamic memory allocation. FEM meshes with a graded step are used and there is more freedom in automatic fine mesh generation. Old type of data for FEM or tracing can be imported. In the background the geometry of other data can be shown as well as CAD DXF files, to which the coarse mesh can snap. The program displays axial potential or field and/or color-coded saturation of iron or map of potentials or fields [4].

Recently we concentrated on the computation of optical properties from paraxial trajectories and aberration integrals for systems with lenses and deflectors. Let us stress that, in accurately computed fields, the ray tracing of suitably chosen set of rays provides paraxial properties as well as aberrations of any order. The number of data produced while ray tracing is quite large and there is a need to establish safe and easy to use procedures for the display of results and processing of ray tracing results for a given purpose such as the evaluation of given set of aberrations.

Future development of EOD will be aimed not only at improving further the input and output of ray tracing, to extracting aberration coefficients from ray tracing results, analyzing spot profiles and emittance diagrams. For example, the analysis of complex systems should allow

a routine computation of optics of mirror and multipole correctors, the analysis of dynamic corrections of aberrations of high accuracy deflection systems and the analysis of misaligned systems, and eventually later even stochastic Coulomb interactions or interactions of the beam with gas. [5]

References:

[1] B. Lencová, Proc. Recent trends (9th seminar), Brno 2004) 43-46.
[2] B. Lencová, J. Zlámal, Proc. EUREM 2000, Brno, Vol. I, 101-102.
[3] P. Jánský, B. Lencová, J. Zlámal, Proc. MC2003, Dresden, 22-23.
[4] B. Lencová, J. Zlámal, Proc. MC2005, Davos, 8.
[5] Supported by the Institutional Research Plan No. AV0Z20650511 of AS CR.

Figure 1: Example of some of the windows displayed to analyze a 2-tube lens: geometry – output of field and equipotentials – tracing of trajectories and computation of paraxial properties and aberrations.

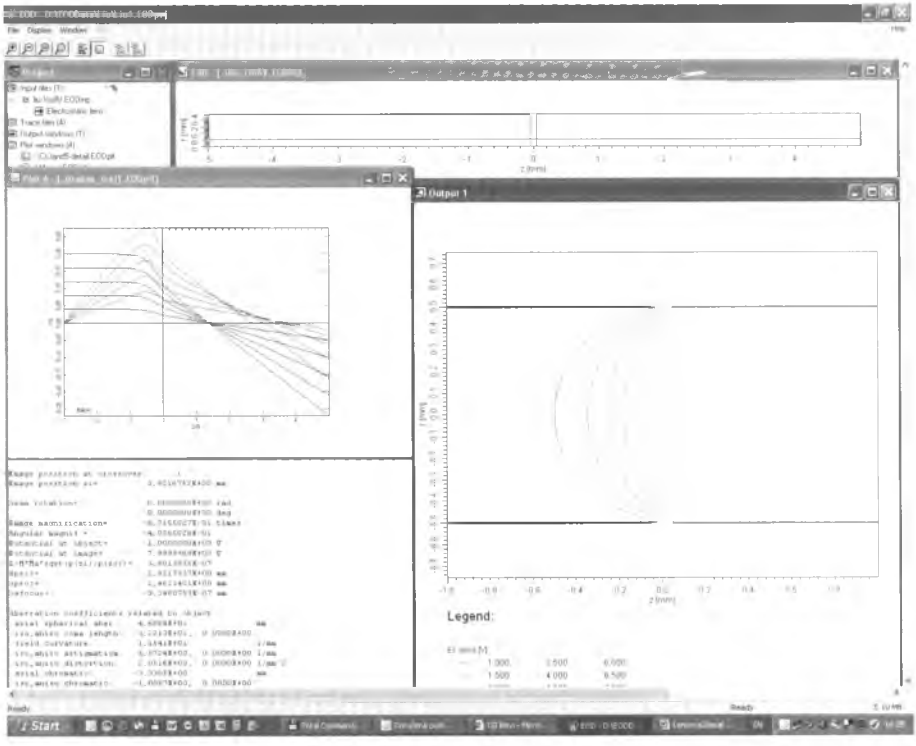

IMAGING OF DOPANTS IN SEMICONDUCTORS WITH THE SECONDARY ELECTRONS IN A LOW ENERGY SEM

F. Mika and L. Frank

Institute of Scientific Instruments ASCR, Královopolská 147, 612 64 Brno, Czech Republic
fumici@isibrno.cz

One of the crucial parameters in characterization of semiconductor devices is the dopant distribution profile. Dimensions of the doped structures have decreased to the 10^2 nm level, so details in both lateral and in-depth distributions of dopants fall at least in the same order of magnitude. Consequently, the device characterization becomes a non-trivial task. Two-dimensional dopant profiling in this study was made in the cathode lens equipped low energy scanning electron microscope (LESEM). In addition to non-destructive imaging and availability of multiple signal modes, advantages of this type of the LESEM include very efficient signal collection and hence high speed of data acquisition. The dopant profile is determined upon magnitude of the secondary electron (SE) signal [1], namely by measuring the image contrast between doped areas and the substrate.

The contrast mechanism has been interpreted in terms of electric fields above [2] or below [3,4] the surface, variations in energy and angular distributions of the SE emission [4,5], and recently the primary electron dose delivered to the surface was taken into account, too [6,7]. This study aims at examining the contrast behaviour as a function of the angular and electron dose factors on two series of samples. Set *A* was with the p-type doped patterns (1×10^{16} to 1×10^{19} cm^{-3} of boron atoms) made on an Si (100) n-type substrate (1×10^{15} cm^{-3} of phosphorus atoms), and the set *B* had the opposite conduction types. Surface topography was checked in the AFM device, which revealed the steps on boundaries between the doped areas and substrate to be only 6.3 nm in height for the set A, and 36 nm for the set *B*.

Both sets of the semiconductor wafers, exposed to the same history of aging, were observed in the as-inserted status in a Vega TS 5130MM microscope. The landing electron energy was 1 keV and the image signal was collected with a standard Everhart-Thornley detector (ET) and with the cathode-lens detector (CL). At low magnifications and fast scan rates the p-type silicon appears brighter in the SE emission than the n-type Si (Fig. 1). As usually in standard-vacuum microscopes, any increase in magnification or decrease in the scan speed lead to more intensive contamination of the field of view with carbon, and also the local charging is more apparent. In the same time, decrease or even reversal of the contrast between differently doped areas is observed. With the set *B*, the contrast reversal has been found dependent on the electron dose (Fig. 2) while for the set *A* only some decrease in contrast was established. No clear explanation of the contrast reversal is available yet. Let us add that the samples freshly cleaned in HF exhibit a monotone contrast development without inversions.

Imaging in the cathode lens mode indicated the contrast behaviour possibly connected with differences in the angular distribution of the signal emission. When comparing a micrograph acquired with the CL detector well axially aligned and hence not collecting the near-axis emission that escapes through the central hole (Fig. 3a) with the identical field of view as recorded with the detector laterally misaligned by about 100 μm, which enlarges collection of electrons emitted near the axis (Fig. 3b), we meet the contrast inversion again.

Information collected so far obviously extends the scope of factors, connected with technology of preparation of the structure, its treatment before observation, environment in the microscope chamber, up to properties and intensity of the illuminating beam, which have to be taken into account if the image contrast of doped areas should be reliably (and even quantitatively) predicted and also utilized in diagnostic tasks.

[1] Perovic, D. et al. *Ultramicroscopy* 58 (1995) 104.
[2] Sealy, C. P. et al. *J. Electron Microsc.* 49 (2000) 311.
[3] El-Gomati, M. M. et al. *IEEE Trans. Electron Dev.* 51 (2004) 288.
[4] Müllerová, I., El-Gomati, M. M., Frank, L. *Ultramicroscopy* 93 (2002) 223.
[5] Schönjahn, C. et al. *Appl. Phys. Letters* 83 (2003) 293.
[6] Mika, F., Frank, L. *PSI Proceedings 05-01* (2005) 50.
[7] El-Gomati, M. M. et al. *Surf. Interface Anal.* 37 (2005) 901.
[8] The work is supported by the Grant Agency of CR under grant no. GA102/05/2327.

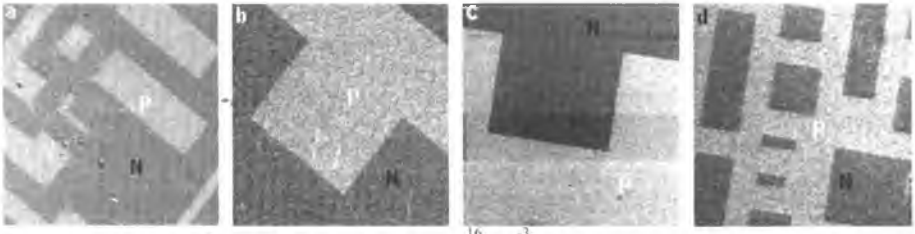

Figure 1: ET detector imaged p-type doped (1×10^{16} cm^{-3}) patterns on an n-type substrate (1×10^{15} cm^{-3}) (a), structure with the opposite conduction types (b), the two struetures with the dopant concentrations increased to 1×10^{18} cm^{-3} (c,d).

Figure 2: Contrast reversal as a function of the electron dose:(a) 147 pCcm^{-2}, (b) 294 pCcm^{-2}, (c) 440 pCcm^{-2}; (d) detail of the inverted contrast image, dose 8.72 μCcm^{-2} (n-type doping 10^{19} cm^{-3}, ET detector at 1 keV).

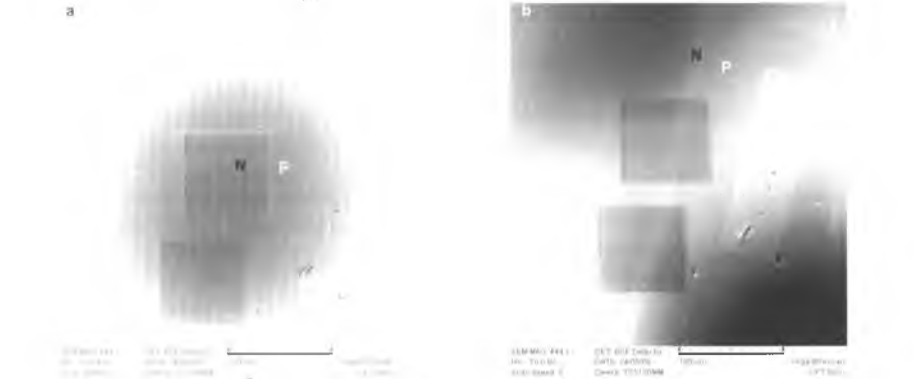

Figure 3: N-type 10^{19} cm^{-3} sample imaged with the CL detector at 1 keV: (a) deteetor aligned on the axis, no inversion in the centre of the picture; (b) off-axis shifted detector, n-type emission increased and dominates.

CATHODE LENS MODE IN THE SCANNING ELECTRON MICROSCOPE

I. Müllerová

Institute of Scientific Instruments ASCR, Královopolská 147, 612 64 Brno, Czech Republic, e-mail: ilona@isibrno.cz

The Cathode Lens (CL) mode of the Scanning Electron Microscope (SEM) seems to start attracting attention of developers as well as users of the microscopes. Based upon our nearly 15 years experience with this experimental principle, mostly summarized in [1], a brief recapitulation of usefulness of this system is presented here.

Electron optical calculations show [2] that the only way of obtaining the high resolution in an SEM at very low energies (below 100 eV) is to use the CL principle, in which the sample is immersed in strong electrostatic field and forms the cathode of this electrostatic lens. When adapting a conventional SEM, a feasible solution consists in employing a sequential arrangement of the electrostatic field of the CL and magnetic field of the focussing lens with only weak magnetic field appearing in the specimen plane. The CL anode serves as a single-channel dark-field detector made from the YAG crystal with a small central opening (say, 0.3 mm) enabling passage of the primary beam. This detector is inserted between the specimen and polepiece of the objective lens, requiring hence a relatively large working distance (usually above 5 mm) as its main disadvantage. Calculated and measured spot size versus landing energy of electrons for one example of this simple adaptation of the SEM to the SLEEM (Scanning Low Energy Electron Microscope) mode is shown in Figure 1. Here the spot size was calculated by using approximate analytical equations [3] and aberrations of the combination of CL and focusing lens resulted from analytical equations [4].

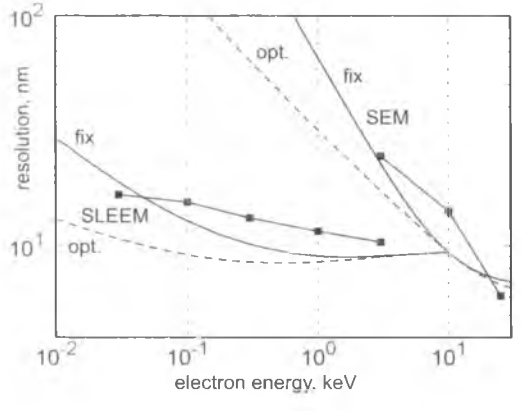

Figure 1: The energy dependences of the spot size calculated for aberration coefficients of the magnetic focusing lens C_S = 10 mm and C_C = 12 mm; primary beam current was 5 pA, gun brightness 10^5 A cm^{-2} sr^{-1}, primary beam energy 10 keV and energy spread 2 eV; the fixed aperture was 8 mrad. The image resolution, measured as a 25/75 edge width on the standard Au/C testing sample in the Hitachi S-3500H SEM adapted to the SLEEM mode, is marked by points.

In modern high-resolution SEMs the specimen is immersed in strong magnetic field in order to secure the ultimate resolution, and detectors are mostly placed above the objective lens so that the working distance is preserved small. Should the CL mode be introduced, the specimen finds itself in both magnetic and electrostatic fields, namely strong and overlapped. Some data about aberration coefficients and probe diameters for overlapped as well as sequential configuration of the fields have been published [5]. We have measured the image resolution for the overlapped fields and arrived at 9 nm for 10eV [6]. The overlapped fields surely promise better resolution than sequential ones but signal electron trajectories become more complicated so explanation of the contrast formation is more difficult.

In the case of sequential fields a multi-channel position-sensitive detector can be designed rather simply [7] because the emitted electrons keep their azimuthal angle when collimated to the optical axis by the CL electrostatic field, in accordance with initial energy and polar angle. In the overlapped electrostatic and magnetic fields the task becomes more difficult. Still, our preliminary calculations [8] showed that the immersion lens, formed by a single pole-piece lens and the CL, transports at very low landing energies relatively well a broad range of initial angles of the signal trajectories so that the diffraction contrast can be obtained similarly as in sequential fields. When varying the landing energy of electrons via the CL potential by orders of magnitude, e.g. from 10 keV to 10 eV, the necessary (not too large) refocusing even increases the objective lens excitation [1]. Thus, the CL mode in a high-resolution SEM implies the both specimen-surrounding fields growing toward lowest landing energies. However, as regards action on electron trajectories the electrostatic field keeps dominating [9].

Figure 2 shows the gold-on-carbon resolution-testing specimen in the SLEEM mode at various landing energies, both with overlapped and sequential fields [6]. In the overlapped fields at very low energies the topographical contrast is more or less preserved but the material contrast is lost. This indicates the angular information about the specimen as transported relatively well, contrary to the energy information. Detailed interpretation of contrasts acquired in the overlapped field configuration will require additional calculations and experiments to be done.

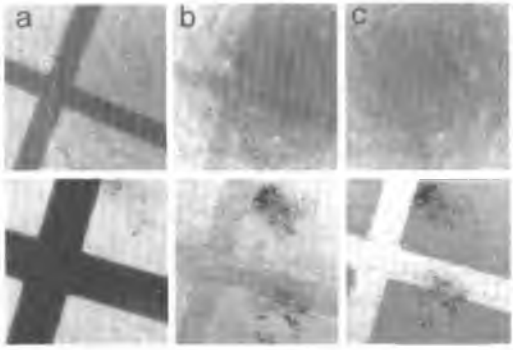

Figure 2: Micrographs of the gold/carbon testing specimen (Agar S169T) taken at the landing energies: a) 3020 eV, b) 320 eV, c) 20 eV. Upper row: overlapped fields, bottom row: sequential fields; primary beam energy 10 keV, width of the field of view 0.1 mm (upper row) and 0.2 mm (bottom row). (Reproduced from [6].)

At very low energies below 100 eV the SLEEM mode offers similar contrast mechanisms (see e.g. [10, 11]) as the LEEM instrument [12]. However, experience has showed the CL mode in the SEM very fruitful even at medium energies, say around 1 keV. For example, an optimum landing energy can be found for non-charged imaging of a majority of non-conductive uncoated samples [13] or at least the charging can be strongly reduced. This method can be useful e.g. for observation of insulators and/or in-situ treated samples under ultra-high-vacuum conditions. The above-mentioned simple multi-channel detector of the angular distribution of emitted electrons, designed with the CL anode inserted between specimen and pole piece of the objective lens and above the detector, also works best in the medium energy range. Figure 3 shows the patterned collector, placed behind a micro-channel-plate, together with calculated trajectories [7]. Obviously, even trajectories originating under largest polar angles are collected but application to high immersion ratios, i.e. low landing energies, would bring the strongly collimated signal electron trajectories escaping the detection through the central bore. A tailored design of an above-the-lens and off-the-axis detector is needed for this purpose [14]. In this context, let us remember that in the CL mode the complete energy spectrum of emitted electrons is accelerated to its upper end fitting the

primary beam energy, so very high efficiency of the scintillator or semiconductor detectors is secured at low landing energies.

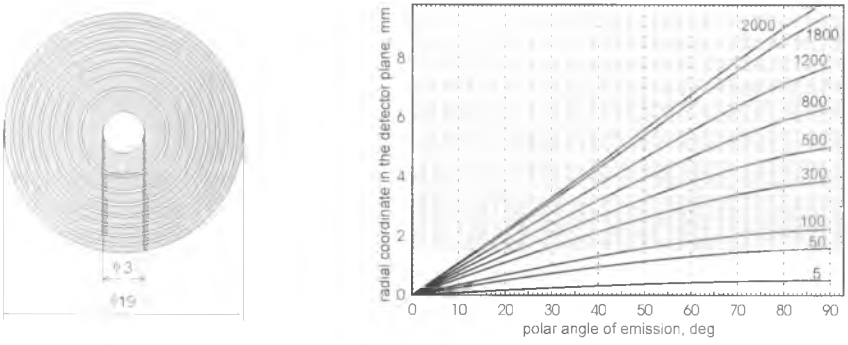

Figure 3: Left: eight-channel collector of a multi-channel detector. Right: the radial coordinate in the detector plane versus initial polar angle of the signal trajectory; primary energy 10 keV, landing energy 2 keV, distance between the cathode (specimen) and anode (detector) is 10 mm, curves labelled with the emission energies, detector segments indicated as the grey strips. (Reproduced from [7].)

Further indisputable advantage of the low, but also of the medium energy range is the interaction volume proportionally diminishing, opening hence possibilities for a kind of layer by layer in-depth tomography [15]. The SLEEM method was used for investigation of the cube phase in an Al-Mg-Si alloy [16]. In these experiments, visibility of nanometre-sized precipitates without any surface relief was very clear thanks to small spread of electrons, advantageous mixture secondary and backscattered electrons, and enhanced crystallinity contrast. Consequently, multiple types of precipitates have been recognized in these micrographs (Figure 4), as distinct from the standard SEM.

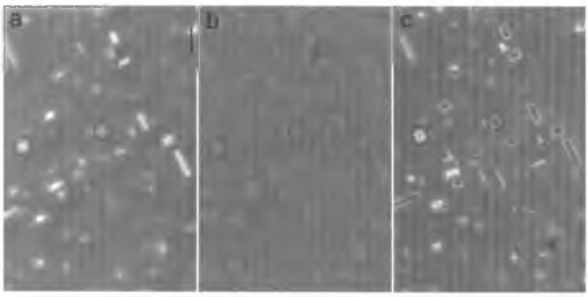

Figure 4: Surface of an age-hardened Al-1.0 mass%Mg_2Si alloy with 0.4% excess Mg, observed in (a) SE at 10 keV, (b) BSE at 10 keV, and (c) SLEEM at 1600 eV landing energy and 10 keV primary energy; the scale bar is 1 μm long. (Reproduced from [16].)

The contrast interpretation issues can be illustrated on doped areas in semiconductors [18]. In the example in Figure 5 two pictures are taken by so-called lower and upper SE detector [19] with the specimen immersed in the magnetic field while the other two snaps show the same field of view in the CL mode, i.e. with the specimen situated in both fields in an overlapped arrangement. Thus, we have four images, all taken at 1 keV landing energy but acquired with four different detectors. As regards the CL mode, difference was only in diameter of the central bore and consequently in the angular range acquired.

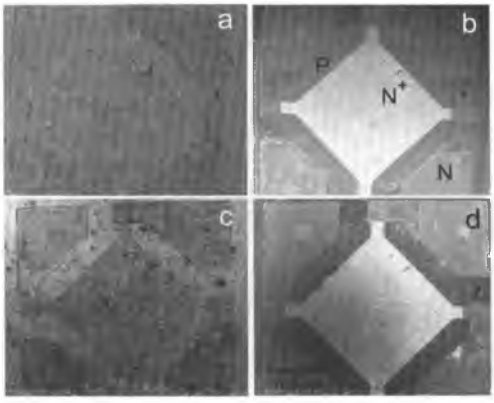

Figure 5: Patterned diffusions into Si (111) substrate, imaged at 1 keV landing energy by means of four detectors in the JEOL 6700F SEM adapted to the CL mode: (a) lower and (b) upper standard SE detector, the SLEEM detectors of central bore of (c) 1.7 mm and (d) 0.3 mm in diameter; primary beam energy 10 keV, landing energy in the SLEEM mode again 1 keV. (Reproduced from [17].)

We can conclude that reliable interpretation of contrasts requires knowing in detail what part of the angular and energy distribution of the emitted electrons is collected and what is the efficiency of the subsequent signal processing. This rule holds generally for the SEM but in the medium and low energy modes more information is transmitted in the emission distributions instead of mere total yields. [20]

[1] Müllerová I. and Frank L.: In: Advances in Imaging and Electron Physics **128** (ed. P.W.Hawkes), San Diego: Elsevier (2003) 309-443.
[2] Frank L. and Müllerová I.: J. Electron Microscopy **48** (1999) 205-219.
[3] Barth J.E. and Kruit P.: Optik **101** (1996) 101-109.
[4] Lenc M.: In: Proc. MCEM, ed. by F. Čiampor, Bratislava: Slovak Academy Press (1995) 103-104.
[5] Khursheed A.: Optik **113** (2002) 67-77.
[6] Müllerová I. and Frank L.: Scanning **25** (2004) 18-24.
[7] Müllerová I. and Konvalina I.: In: Proc. Microscopy and Microanalysis 2006, Chicago, in print.
[8] Müllerová I. and Lenc M.: Mikrochimica Acta [Suppl.] **12** (1992) 173-177.
[9] Müllerová I., Lenc M. and Fišer J.: In: Proc. 10th ECEM, vol.1, ed. by A. Rios et al, Granada Spain (1992) 63-64.
[10] Frank L., Müllerová I., Faulian K. and Bauer E.: Scanning **21** (1999) 1-13.
[11] Frank L. and Müllerová I.: Ultramicroscopy **106** (2005) 28-36.
[12] Bauer E.: Rep. Progr. Phys. **57** (1994) 895-938.
[13] Frank L., Zadražil M. and Müllerová I.: Scanning **23** (2001) 36-50.
[14] Vlček I., Lencová B. and Horáček M.: In: Proc. 9th International Seminar Recent Trends in Charged Particle Optics and Surface Physics Instrumentation, ed by Müllerová I., Brno, ISI AS CR (2004) 75-76.
[15] Rau E.I. and Reimer L.: Scanning **23** (2001) 235-240.
[16] Matsuda K., Ishida Y., Müllerová I., Frank L. and Ikeno S.: Solid-to Solid Phase Transformations in Inorganic Materials. Vol.1: Diffusional Transformations (2005) 371-376.
[17] Müllerová I. and Frank L.:In: Proc. 13th ECM, Liege, Belgien Society for Microscopy (2004) 323-324.
[18] Müllerová I., ElGomati M.M. and Frank L.: Ultramicroscopy **93** (2002) 223-243.
[19] Kazumori H.: JEOL News **37E**(1) (2002) 44-47.
[20] The work is supported by the Czech Science Foundation under grant no. 102/05/2327. Mr. Matějka of ISI Brno kindly provided the specimen of the semiconductor structure.

DIFFERENTIAL ALGEBRAIC METHOD FOR ELECTRON OPTICAL DESIGN

Eric Munro, Liping Wang, John Rouse and Haoning Liu

Munro's Electron Beam Software Ltd, 14 Cornwall Gardens, London SW7 4AN, England
e-mail: eric@mebs.co.uk Tel & Fax: +44 20 7581 4479

The Differential Algebraic ("DA") Method [1, 2] is a powerful and elegant technique for computing the aberrations of electron optical systems. It is far more powerful than traditional methods based on evaluation of aberration integrals. It is particularly useful in the following situations: (1) Evaluation of high order lens aberrations (5^{th}, 7^{th} order, etc.), (2) Aberrations of multipole systems, including Wien filters, (3) Curved axis systems, such as prisms, spectrometers and energy filters, (4) Electron mirrors, (5) Evaluation of asymmetry aberrations, and (6) Systems with high beam energy, where relativistic effects are significant.

The DA method is conceptually quite simple. We define a ***Differential Algebraic Quantity*** ("***DA Quantity***"), of degree n in v variables, using the notation "${}_nQ_v$". The quantity ${}_nQ_v$ is a vector whose elements are the coefficients of a polynomial of degree n in the v variables. We also define a set of ***Algebraic Operations*** on pairs of DA quantities. Addition, C=A+B, is defined as the addition of the two polynomials. Multiplication, C=A×B, is defined as the multiplication of the two polynomials, discarding terms of degree greater than n. Subtraction, Division, Square Roots, etc., are also defined, to form a complete Algebra. In software terms, DA quantities form a new ***Data Type***, which we call **DA**, with its own storage structure and operations, which we have programmed as a ***C++ Class***. We can then write statements in our program like F = ((A+B)*C – sqrt(2.0*D)/E, where the variables A – F are DA Quantities.

These DA quantities dramatically simplify our software for computing aberrations. To obtain the aberrations, we need the electron's final position (x_i,y_i) and final slope (x_i',y_i') at the image plane z_i, as a power series in powers of its initial position (x_o,y_o), initial slope (x_o',y_o') and initial energy deviation $(\delta\Phi)$ at the object plane z_o. To express the aberrations as a power series in these 5 variables – $(x_o, y_o, x_o', y_o', \delta\Phi)$ – we use DA Quantities in 5 *variables*, i.e. $v = 5$. The *degree* n of the DA Quantities is chosen as the maximum aberration order we wish to compute. For example, if we require the aberrations to 7^{th} order, we choose *degree* $n = 7$.

We write out the differential equations of motion, which describe an electron's position $(x(z), y(z))$ and slope $(x'(z), y'(z))$ as functions of its axial position z, under the influence of the electrostatic and magnetic fields. These equations are written in curvilinear coordinates so we can handle general curved axis systems. In these equations, we replace the physical position and slope by their equivalent DA Quantities – X, Y, X', Y'. We also replace the physical electric and magnetic field components by DA Quantities. We fit the numerically computed axial field functions with sets of Hermite functions [3], which are continuously differentiable analytic functions. This is a crucial step, as the DA Method requires the fields be analytically defined and differentiable. We now solve the equations of motion, ***with a single raytrace***, from object plane z_o to image plane z_i, using a Runge-Kutta method. The code is a standard Runge-Kutta solver, except that all simple variables are replaced by DA Quantities. On completion of the single raytrace, the DA Quantities X, Y, X', Y' contain all the position and slope aberration coefficients at the image plane. ***This is all achieved without any derivation of aberration integral formulae***. This makes the software very robust and reliable.

The method can easily be modified to handle cathode lenses and electron mirrors. For this, we start from the equations of motion for the electron's coordinates $(x(t), y(t), z(t))$ and velocity components $(\dot{x}(t), \dot{y}(t), \dot{z}(t))$ as functions of time t, and replace the physical coordinates and velocity components by their equivalent DA Quantities – $X, Y, Z, \dot{X}, \dot{Y}, \dot{Z}$. This eliminates singularities at the turning point, since the electron's coordinates and velocity components are everywhere finite. After a single raytrace, the DA Quantities $X, Y, Z, \dot{X}, \dot{Y}, \dot{Z}$ at the image plane z_i contain all the information about the aberration coefficients, to any required order.

The accuracy has been checked using analytic model fields. Figure 1 shows an example for a combined electrostatic-magnetic diode mirror with 2 cylindrical electrodes of 40 mm diameter and 10 mm gap, and 2 polepieces of 44 mm diameter and 8 mm gap. The fields were computed with Fourier-Bessel series and the primary aberration coefficients were extracted from a raytrace through the analytic fields, for electrons with an initial energy of 6996.2 eV, and object and image points at 107.682 mm to the left of the lens centre. The same data were then computed with the DA method. The errors in the DA results (Table 1) were all < 0.2%.

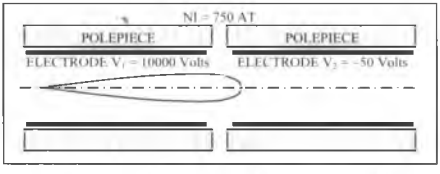

Figure 1. Analytic test with diode electron mirror.

Aberration	Analytic Result	DA Result
Spherical Ab.	51.31	51.30
Coma	−486.1 + 69.58 *i*	−485.9 + 69.51 *i*
Field Curv.	9376	9372
Astigmatism	4517 + 1316 *i*	4514 + 1317 *i*
Distortion	−44335 − 6341 *i*	−44326 − 6342 *i*
Axial Chrom.	−2.618	−2.618
Trans. Chrom.	24.80 + 2.307 *i*	24.80 + 2.309 *i*

Table 1. Computed aberration coefficients (SI Units).

Both the C_s and C_c of an objective lens can be corrected using a tetrode mirror [4]. Figure 2 shows an example of a practical tetrode mirror, simulated with our DA software. The object and image planes were kept fixed at $z = -180$ mm, with an incident beam energy of 10 keV. Voltage V_3 was held at 60 Volts, and for each setting of V_2 the final potential V_4 was varied to adjust the focus. C_s and C_c were computed for each voltage setting (Table 2). C_c is always negative, so it can correct the C_c of an objective lens. C_s can be adjusted over a wide range, from positive to negative, so the C_s of the objective lens can also be cancelled.

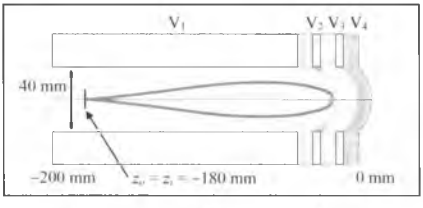

Figure 2. A practical tetrode mirror.

V_1 (Volts)	V_1 (Volts)	V_1 (Volts)	V_1 (Volts)	C_s (mm)	C_c (mm)
10000	100	60	−168.76	+390	−17818
10000	200	60	−159.46	−1209	−17970
10000	300	60	−150.54	−3231	−18215
10000	400	60	−149.94	−5779	−18571
10000	500	60	−133.71	−8666	−19008

Table 2. Computed C_s and C_c values of tetrode mirror.

We will present results showing how a tetrode mirror and prism can correct the C_s and C_c of a real objective lens, with the lens-prism-mirror combination simulated with the DA method.

[1] M. Berz, *Particle Accelerators* **24** (1989) 109-124.
[2] L. Wang, T. Tang and B. Cheng, *Optik* **111** (2000) 285-289.
[3] L. Wang, J. Rouse, H. Liu, E. Munro and X. Zhu, *Microelectronic Eng.* **73** (2004) 90-96.
[4] D. Preikszas and H. Rose, *Journal of Electron Microscopy* **1** (1997) 1-9.

ENVIRONMENTAL SCANNING ELECTRON MICROSCOPE AQUASEM II – THE DESIGN AND APPLICATIONS

V. Neděla[1], J. Maxa[2], R. Autrata[1]

[1]Institute of Scientific Instruments AS CR, Královopolská 147, Brno, Czech Republic, vilem@isibrno.cz
[2]The Faculty of Electrical Engineering and Communication BUT, Údolní 53, Brno, maxa@feec.vutbr.cz

Environmental scanning electron microscope (ESEM) creates new possibilities in the examination of various types of specimens and their phases. Experimental environmental scanning electron microscope AQUASEM II was built in ISI AS CR in cooperation with the TESCAN Ltd. The main task of this microscope is the investigation and development of special detector systems working in high pressure conditions and the study of „in situ" dynamic experiments.

The microscope is equipped with hairpin tungsten filament. The accelerating voltage (AV) can be adjusted from 0.5kV to 30kV and the probe current from 1pA to 2nA. The resolution (high vacuum mode, AV=30kV, working distance =3mm) is 3.5nm, and for ESEM mode (AV=30kV, WD=3mm, specimen chamber pressure 1000Pa) is approximately 10nm. The vacuum system of AQUASEM II consists of two rotary pumps and one turbo-molecular pump. The microscope is equipped with Peltier cooled specimen holder with mechanical movement system in X,Y and Z axis. The pressure values are measured independently of the gas type by the capacitance pressure gauges in the specimen chamber and in the differential chamber.

The differential pumping chamber with detector unit (pressure up to 25Pa) are the main special parts of the microscope that enable to maintain high pressure (up to 2000Pa) in the specimen chamber and vacuum (0.001Pa) in the optical column of the microscope. These parts make additional pumped space situated between the objective lens and the specimen chamber, shown in Figure1. In the small circular hole (diameter approx. 7mm), situated in the centre of the detector unit, is placed with the yttrium aluminium garnet (YAG) single crystal scintillator, the main part of backscattered electron detector. The scintillator is also used as a pressure limiting aperture; a hole with diameter 0.5mm is bored into its centre. The differential chamber, the detector unit and the YAG single crystal are vacuum sealed with "O"-rings. The circular hole through the YAG single crystal must by centred on the optical axis by shifting the detector unit in direction of X,Y axis in the high vacuum mode, see Figure 2. The scintillator is used as the secondary electron detector (SED) [1] for variable pressure and ESEM mode. Secondary electrons are swept by the positive potential around 350V toward the electrode system deposited on the surface of YAG and switched to the current amplifier.

ESEM AQUASEM II is also equipped with a special temperature isolated hydration system situated outside the specimen chamber, see Figure 3. This system consists of water reservoir, water level meter, water vapour temperature meter, heating system with precise temperature controller and precise flow calibrated micrometric valve. This system ensures an efficient replacement of air in the specimen chamber by the water vapour from the hydration system. It also enables to maintain stable high humidity environment respecting the physical dependence of pressure of saturated water vapour on temperature.

ESEM AQUASEM II is a universal experimental microscope for the examination of conductive or non-conductive specimens, specimens in their liquid phase or specimens through their changes in phase. The microscope can by use for dynamical "in situ" experiments [2] such as the time change of, temperature or humidity of the sample or the observation of melting, solidification, dissolution and chemical reaction [3].

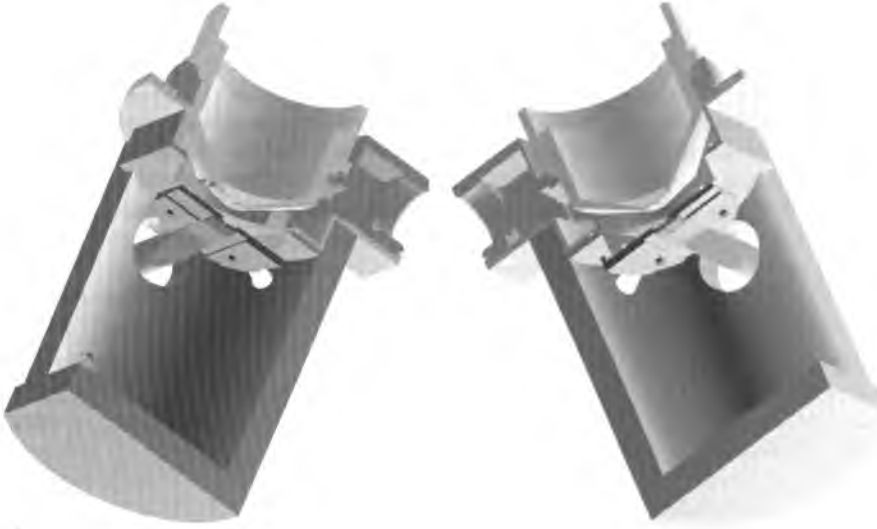

Fig.1. Cut-away view of ESEM AQUASEM II: (from below) specimen chamber, detector unit, differential pumping chamber and a part of the microscope column.

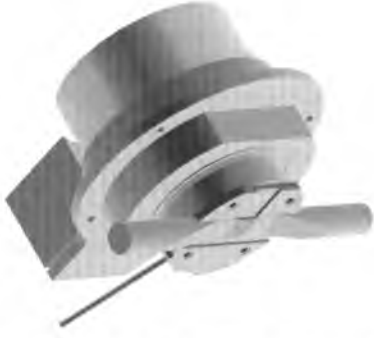

Fig.2. The complete view of the differential chamber with detector unit

Fig.3. Hydration system of ESEM AQUASEM II

[1] Danilatos G.D.: Theory of the gaseous detector device in the environmental scanning electron microscopy. Advances in Electronics and Electron Physics, 78, (1990), 102.

[2] Donald A.M.: The Use of Environmental Scanning Electron Microscopy for Imaging Wet and Insulating Materials. Nature materials 2 (2003) 511-516

[3] This work was supported by Academy of Sciences of the Czech Republic, grant No. KJB 200650602 and by Grant Agency of the Czech Republic, grant No. 102/05/0886.

PROCESSING OF SIGNAL IN THE EVERHART-THORNLEY DETECTOR

L. Novák and I. Müllerová

Institute of Scientific Instruments, ASCR, Královopolská 147, 612 64 Brno, Czech Republic
e-mail: kdovikdo@email.cz

The Everhart-Thornley detector has been used for detection of secondary electrons since 1960 [1]. In order to increase the signal to noise ratio (SNR) in the resulting signal many configurations of this detection system have been developed. The collection efficiency corresponding to a full chamber configuration has become possible to simulate [2] as well as to compute and experimentally test the properties of the scintillator and the light guide [3]. So far description of individual parts of the detection route has been based on signal averages. This approach enables us to analyze the transfer of the signal and simultaneously to assess the noise characteristics of the detection route. As a matter of fact, this method disregards processes participating in the signal formation and besides, it is not applicable to low currents.

A new approach to the above-mentioned problem has been felt necessary in order to incorporate measurement of very small currents ($\geq$0.01 pA) coming into the detector. For experimental study, a special chamber equipped with two E.-T. detectors was fabricated. One of them has the standard position (on a side of the chamber) while the other is directly exposed to the impact of primary electrons. The primary current can be measured by means of a movable Faraday cup. In fact, three parts of the detection route were examined. Using the chamber described, the section starting with scintillator and ending with preamplifier was thoroughly investigated. In order to identify the influence of photomultiplier, its input was excited with a LED signal. Fig. 1 shows a pulse generated by one detected electron at the output of the preamplifier. Finally, the signal-processing electronics was tested by means of a voltage generator.

Two detectors of two different manufacturers have been examined. The main features observable in detection routes of these detectors proved themselves quite similar. Measurements exhibit an exponential decrease in the number of high pulses of light coming out of the scintillator. In the photomultiplier/preamplifier section of the detector the shape of the tranported signal changes in two significant ways. The photomultiplier adds noise pulses whose number is proportional to voltage on the dynodes. In comparison with these pulses the dark current of the photocathode becomes negligible. The preamplifier smoothens the signal according to frequency of the filter chosen. As a result of this, SNR [4] in the output signal can rise but at the same time information about fast changes in the signal (edges, phase contrasts) becomes lost. In terms of the measurement accuracy the signal-processing electronics does not increase the signal noise, introducing quantization noise only, as a result of the digitalization.

Taking into account the above-mentioned properties of the detection route, a computer simulation routine was created in Matlab. This is based on generation of single pulses that represent light pulses leaving the scintillator. They occur randomly but their heights and widths are correlated with the measured values. The artificial signal created in this way is then processed by means of individual operations, such as filtration, addition of noise pulses etc., in line with what actually happens in the detector. Comparison between the real pulses from the detector and the generated ones is pictured in Fig. 2. By dint of the simulation we obtain an image in which the SNR and blurring of edges at fast signal changes can be determined. This makes it possible for us to evaluate the features of the detection route in its totality. The line-scans across real and simulated images are contrasted in Fig. 3. The SNR of the simulated image and of those obtained by means of E.-T. detectors are then portrayed in

Fig. 4. For a given set of parameters describing configuration of the detector, simulation can be performed cyclically. Having processed and classified all combinations of these parameters, an optimum configuration of the detection route can be found.

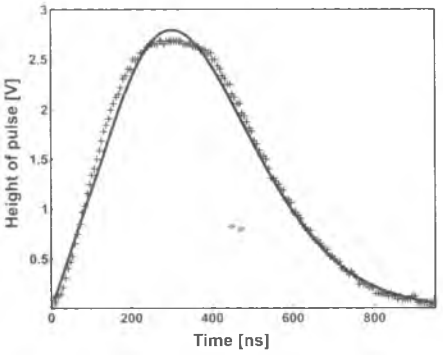

Fig. 1 Crosses – the pulse arising from one deteeted electron acquired at output of the preamplifier. Solid line – fitting by the function $U(t)=c_1.t.\exp(-c_2.t)$ (Filter in the preamplifier - 5 MHz)

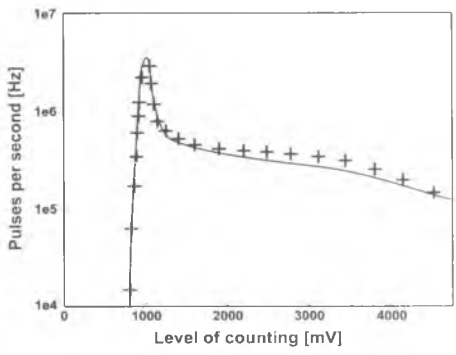

Fig. 2 Crosses –counting of pulses at the output of the preamplifier (U_{acc}=10kV, I_{det}=0.1pA, contrast 30%). Solid line –counting of the simulated pulses.

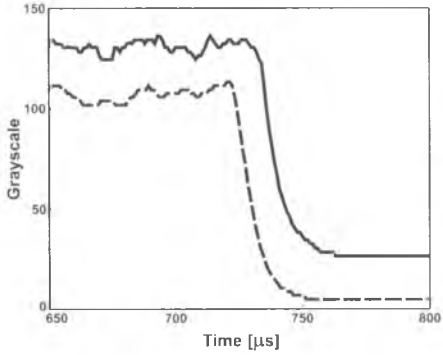

Fig. 3 Solid line – line-scan acquired using an E.-T. detector (U_{acc}=10kV, I_{det}=10pA, dwell time 1μs, contrast 30%, filter 25kHz, fast blanking used). Dashed line – computer simulation of the same line-scan. (Lines were artificially shifted in order the shape of both signals can be discerned.)

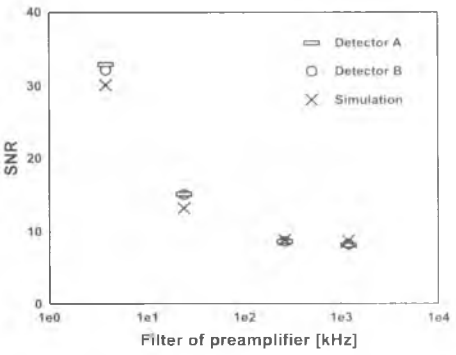

Fig. 4 Circles and rectangles – SNR estimated from the images acquired by means of two different detectors of the E.-T. type. Crosses – SNR counted from the simulated image. (Deteeted current 10pA, four different filters were considered in the preamplifier.)

[1] T. E. Everhart and R. F. M. Thornley, J. Sci. Instrum. 37 (1960) 246.
[2] I. Konvalina and I. Müllerová, Microsc. Microanal. 9 (suppl. 3) (2003) 108.
[3] R. Autrata, P. Schauer, J. Kvapil and J. Kvapil, J. Phys. E: Sci. Instrum. 1978, vol. 11.
[4] D. C. Joy et al., Scanning 18 (1996) 533.
[5] The work is supported by FEI Czech Republic, Ltd., and by the Czech Science Foundation, grant no. 102/04/2144.

METHODS OF DIRECT IMAGING OF THE LOCAL DENSITY OF STATES WITH ELECTRONS

Z. Pokorná and L. Frank

Institute of Scientific Instruments, Academy of Sciences, Královopolská 147, Brno
zuza@isibrno.cz

The electronic properties of modern nanodevices are determined by their electronic structure, the local density of states (LDOS) being one of the key characteristics. Various methods exist for the LDOS mapping with lateral resolutions ranging from macroscopic scale (Photoemission Spectroscopy) to the atomic one (Scanning Tunnelling Microscopy). Taking nanodevices as those having at least one dimension under 100 nm, we require a method probing in the scale of at least tens of nm. Another requirement is that the LDOS should directly depend on the quantity measured with the method in question.

Methods for mapping the LDOS are the following:

Photoemission (and *Inverse Photoemission*) *Spectroscopy* are macroscopic techniques for studying the band structure of occupied as well as empty electronic states. In the latter case, electrons of a well-defined energy are incident on the surface and so injected into empty electronic states above the vacuum level. From there they are de-excited into lower empty energetic states and the de-excitation energy is released as an ultraviolet photon. The energy of the lower state is determined by the difference between the incident electron energy and the energy of the released photon. The UV intensity versus UV photon energy plot gives a qualitative image of the distribution of unoccupied electronic states above the Fermi level. The angle-resolved version of this technique allows the 3D band structure $E(\mathbf{k})$ to be mapped.

The tunnelling current in the *Scanning Tunneling Microscope* (STM) is influenced by the local density of states. According to the Tersoff-Hamann model [1], LDOS of the sample is directly proportional to the measured differential conductivity dI/dV(V), obtained by modulating the tip voltage. The model holds rather exactly at low voltages with respect to work functions of the tip and the sample (about 4 eV). However, the model generally requires s-like tip states, and although quantitatively correct concerning the spatial distribution of the LDOS, it is only qualitatively correct concerning the energy dependence. The energy resolution is inversely proportional to the temperature, which is why very low temperatures are used in the experiment.

Under certain specific conditions, the *Scanning Near-field Optical Microscopy* (SNOM) has also been used for the LDOS mapping [2].

Another approach to determination of electronic bands above the vacuum level is to measure the electron reflectivity R(E) by means of the *Very-Low-Energy Electron Diffraction* (VLEED), or the electron transmission T(E) by means of a closely related method of the *Target Current Spectroscopy* (TCS). Both methods employ an electron beam of kinetic energy E in the range of 0 to 30 eV, directed onto a sample surface. In VLEED the elastically reflected current is measured as a function of E, while in TCS the absorbed (transmitted) current is measured. The inelastic contribution varies very little in this energy range, so both R(E) and T(E) contain information about elastically scattered electrons, thus revealing band structure features [3]. Analysis of the data is based on the matching approach of the LEED theory [4,5]. The periodicity of the surface implies that the impinging electrons will only couple to the Bloch states having the same reduced wave-vector component $\mathbf{k}_\parallel$ parallel to the surface. These Bloch states determine, through the matching on the surface, the amplitude of the reflected wave. For example, if for given E and $\mathbf{K}_\parallel$ of the impinging electron wave there

are no free states available, all electrons will be reflected back by the surface, provided that inelastic processes can be neglected. Quantitatively, the relation between the band structure and the reflectivity becomes clear in the surface Green function formalism [6].

The *Scanning Low-Energy Electron Microscopy* (SLEEM) method is a direct descendant of the TCS and VLEED methods. It lets the low-energy electron beam, again with energy below 30 eV, scan over the sample surface, rendering an image of low- and high-electron-reflectivity areas. Tuning the energy of the incident electrons over the 0-30 eV range can then e.g. show contrast changes between grains of different crystal orientation in a polycrystalline metal sample, issuing from their different electronic strueture (Fig. 1).

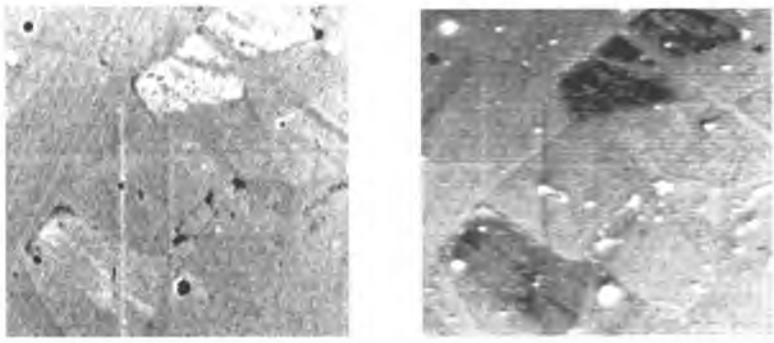

Figure 1: First observation of the contrast changes between differently oriented grains in nickel, energy of incident eleetrons 29 eV and 19 eV, respectively. The sample was rolled and annealed to achieve the desired grain size, and then polished and etched to reveal the grain boundaries.

Applicability of the SLEEM method for direct mapping of LDOS is the topic of the present study. The main issues inelude managing of the non-negligible angular aperture of the incident beam and even of the rocking connected with beam scanning over the field of view. These conditions resemble on those met at the *Convergent Beam Electron Diffraction* (CBED) technique employed in the scanning transmission EM and require the contrast forming model to be reconsidered.

[1] Tersoff, J. and Hamann, D.R., Phys. Rev. B 31 (1985) 805.
[2] Chicanne, C. et al., Phys. Rev. Lett. 88 (2002) 7402.
[3] Strocov, V.N. and Starnberg, H.I., Phys Rev B 52 (1995) 8759.
[4] Pendry, J.B.: *Low Energy Electron Diffraction* (Academic Press, London,1974).
[5] Capart, G., Surf Sci. 13 (1969) 361.
[6] Velicky, B. and Bartos, I., J. Phys. C 2 (1971) L104.
[7] The study is supported by the Grant Agency of CR under grant no. 202/04/0281.

COULOMB INTERACTION IN ION AND ELECTROM BEAMS

T. Radlička

Institute of Scientific Instruments, AS CR Královopolská 147, 612 64 Brno, Czech Republic
radlicka@isibrno.cz

The development of nanotechnologies in present days is often connected with the use of high density ion or electron beams. Unfortunately the physical description of such beams leads into great difficulties, because in high density beams the particle-particle interactions become significant. We can proceed in two main ways, the space-charge method or discrete Coulomb interactions.

The space-charge method was implemented into computer programs [1,2] and is used mainly in high density beams, where the effect of Coulomb interactions may be averaged into an additional field. A disadvantage of the method is that it is not, in principle, possible to describe changes in the energy distribution. When we decide to calculate the Coulomb interactions directly from Coulomb's law as a many-particles problem [3], the energy distribution can be calculated very easily but the calculation time will be much longer.

The first Monte-Carlo calculations of particle-particle interactions in beams were started in the late eighties in TU Delft by Jansen [3]. He described electron beams in free space or in a uniform electrostatic field and used Monte-Carlo method to calculate the beam properties like energy distribution and trajectory displacement. The calculation time even in this simple case was very long. The computers have become much faster in the last 20 years and we can now easily calculate more problematic systems like ion sources. Such calculations also take a long time, but it is possible to do it in several days or week on a PC. The Monte-Carlo method was implemented into a computer code by Munro [4] but it cannot be used for particles in the vicinity of the source.

The simulations of any system consists of four steps

- Calculation of the field in the system. We used FEM programs [5,6].
- Assignment of initial conditions to all particles (position, velocity and time of emission) so that the macroscopic properties of the simulated beam correspond to the properties of a real beam – Monte Carlo methods [7]
- Ray racing of the particle beam in the field including the particle-particle interactions. During calculation the position and velocity of particles at the transition through selected planes are stored for later use.
- Analysis of the beam properties from calculated data.

The ray tracing is the longest and the most problematic part of the calculation. The equation of motion for the i^{th} particle reads

$$m\frac{d}{dt}(\gamma\vec{v}_i) = q\vec{E}_i + q\vec{v}\times\vec{B} + q^2\sum_{j\neq i}\frac{\vec{r}_i - \vec{r}_j}{\left|\vec{r}_i - \vec{r}_j\right|^3}$$

We use the non-relativistic approximation ($\gamma = 1$) for ion systems.

The length of calculation is affected by two properties. The first one concerns the regions where the field is very strong. Even if they may be very small, it becomes a great problem if we consider particle-particle interactions, because all particles must be calculated

simultaneously. In case of calculation of a single particle the integration method will use for each particle that is in a weak field long integration step. However when the evolution of all particles is calculated, the step size is determined by the beam particles that are in a strong field, so it remains very small. Sometimes it is advisable to separate the description of the particle motion in the regions where the field is strong from the rest of the system.

The second limiting property is the number of particles in the system. The Coulomb particle sum is actually an $O(N^2)$ algorithm, which is too lengthy for more than 2000 particles. There are two possible ways how to deal with it. One can cut the system into small parts that are computed independently so that in each part will be on average up to 2000 particles. The second way is to calculate the beam by groups up to 2000 particles. These groups can be bounded from both sides by border particles that are not considered in analysis. The amount of border particles is chosen so that no beam particles will get in front of the first border particle and behind the last border particle.

We simulated two systems, the gallium liquid metal ion source (GaLMIS) and an electron beam lithography (EBL) system. In the case of GaLMIS, the particle-particle interaction were calculated up to 0.1 mm from the source (the beam is very divergent). The evolution was calculated by parts (500 particles) with 200 border particles. In particular we analyzed the energy width (FWHM) at the aperture plane and the virtual source size. In the case of the EBL machine we calculated the effect of particle-particle interactions on the formation of a variable shaped beam of 15keV electrons.

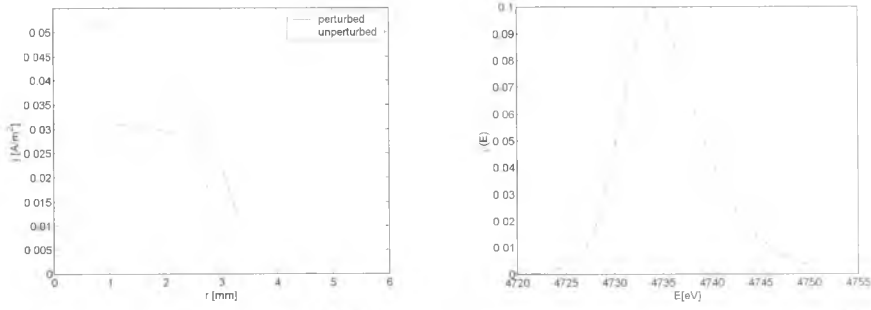

Calculated beam profiles and energy distribution of the beam in Ga LMIS in the aperture plane (at a distance 15mm from the source)

References:

[1] F. Read, N Bowring: Nuc. Inst. and Meth. in Phys. Res. A **519**, 196-204 (2004)
[2] Lencová B, Zlámal J.: Microscopy Conference 2005, Davos, p. 8 (2005)
[3] G.H. Jansen: Coulomb Interactions in Particle Beams, PhD Thesis -- TU Delft (1988)
[4] Munro Electron Beam Software, http://www.mebs.co.uk/
[5] MATLAB 6.5, http://www.mathworks.com/
[6] Lencová B: J. Microsc. **179** (1995), 185-190
[7] W.H. Press, S.A. Teukolsky, W.T. Vetterling, B.P. Flannery: Numerical Recipes in Fortran, Cambridge U. Press (1986)

DECAY KINETICS OF SCINTILLATION CRYSTALS FOR SEM ELECTRON DETECTORS

P. Schauer

Institute of Scientific Instruments, AS CR, Brno, Czech Republic, petr@isibrno.cz

1. Introduction

The principal quantities of image quality in SEM are contrast, spatial resolution, and noise. However, to quantify the overall performance of an imaging system, the detective quantum efficiency (DQE) is a better tool as it includes both the modulation transfer function and the noise power spectrum. This means that for a detector to have high DQE, it should possess not only high efficiency and low noise, but also good kinetic properties. A study of the decay kinetics of some single crystal scintillators for SEM is presented in this paper.

2. Cathodoluminescence decay measurement

The pulse mode utilizing a blanking system and 10 keV electrons for the excitation and a sampling oscilloscope for the cathodoluminescence (CL) detection were used for the measurement of decay characteristics [1]. The measurement was controlled using the IEEE-488 interface and processed by software written in Microsoft Visual Basic. Single crystals of cerium-activated yttrium aluminum garnet (YAG:Ce), cerium-activated yttrium aluminum perovskite (YAP:Ce), cerium-activated yttrium silicate ($Y_2SiO_5:Ce^{3+}$), and europium-activated calcium fluoride ($CaF_2:Eu^{2+}$) were the scintillators studied as the most interesting ones for SEM.

Some typical CL decay characteristics of single crystals for SEM measured in our laboratory are shown in Fig. 1. The best decay characteristic belongs to the P47 single crystal, whose decay time is 34 ns. YAP:Ce single crystal, having the decay time of 38 ns, is also a very good solution. It has, however, a multi-exponential decay characteristic, so it shows the afterglow of 1 % (measured 5 μs after the end of excitation). If a scintillation detection system in SEM is to be able to operate at TV rates, its decay time should be smaller than 100 ns. Hence, the decay characteristic of YAG:Ce is a little problematic. Having the decay time of 110 ns, it shows the afterglow as high as 2 %. Eu-activated calcium fluoride has the decay time of approximately 1.2 μs, and it is applicable only in slow scan rates.

It can be seen in Fig. 2 that the short-term decay component (decay time) of both YAG:Ce and YAP:Ce single crystals depends only negligibly on the duration of excitation. On the contrary, the long-term component of the decay characteristic depends strongly on the duration of excitation. Therefore, at a very short excitation, the afterglows of YAG:Ce and YAP:Ce are one and two orders smaller, respectively, comparing with a long excitation.

3. Kinetic model

It is evident, after a deconvolution of the decay characteristics from Fig. 2, that not only emission from the Ce activator is present in the CL recombination processes in YAG:Ce and YAP:Ce single crystals. Using the correction for the decay constant of the measuring device, the fastest decay constants at whichever duration of excitation are about 60 ns and 20 ns for the YAG:Ce and YAP:Ce, respectively. This corresponds to the single-exponential decay at the photoluminescence measurement [2]. Therefore, the fastest decay constant of the multi-exponential decay characteristic can be ascribed to the emission from the activator. The other decay constants can be ascribed to both radiative and nonradiative transitions originating from unwanted defect and impurity centers. Utilizing the presented results and other CL measurements (first of all dependences of intensities and decays of spectral peaks on the activator concentration), a schematic kinetic model of radiative and nonradiative transitions in the YAG:Ce single crystal has been created in Fig. 3.

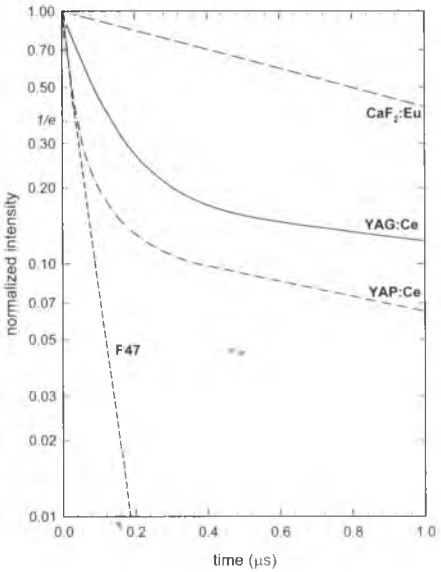

Fig. 1. Cathodoluminescence decay characteristics of single crystal scintillators for SEM. The excitation pulse width was 10 :s.

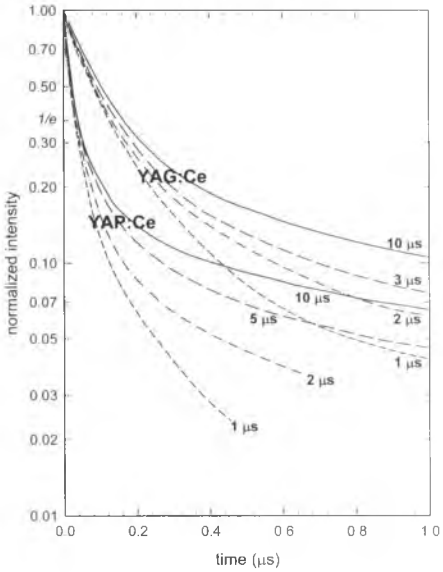

Fig. 2. Influence of the excitation pulse width on the cathodoluminescence decay of YAG:Ce and YAP:Ce single crystal scintillators.

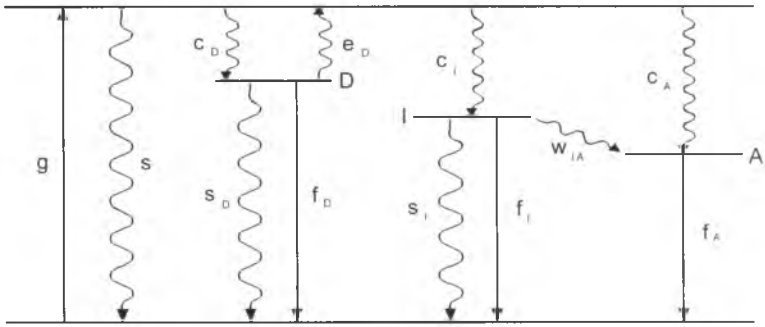

Fig. 3. The kinetic model of the cathodoluminescence of the YAG:Ce. g represents the exciton generation rate; e_D is the thermalization rate from the defect centers; c_D, c_I, and c_A are the capture rates to the defect, impurity and activator centers, respectively; s, s_D, and s_I are the nonradiative rates from the lattice states, defects and impurities, respectively; w_{IA} is the transfer rate from the impurity to the activator centers, and f_D, f_I, and f_A are the radiative (emission) rates from the defect, impurity and activator centers, respectively.

This work was supported by the grant No. 102/04/2144 of the Grant Agency of the Czech Republic.

References

[1] Autrata, R. and Schauer, P.: Scanning Microsc. Suppl. **9** (1996), 1.
[2] Barzowska, J.; Kubicki, A.; Grinberg, M.; et al.: Acta Phys. Polonica A, **95** (1999), 395.

OBSERVATION OF SPIN WAVES, OPTICAL NEAR FIELDS AND SURFACE-PLASMON OSCILLATIONS BY TIME-RESOLVED PEEM

G. Schönhense

Johannes Gutenberg-Universität, Institut für Physik, D-55099 Mainz, Germany
(e-mail: Schoenhense@uni-mainz.de)

1. Introduction

Fast processes on the sub-nanosecond time scale and transient states in nano-scale electronic systems are attracting high interest in basic and applied research. Full-field PEEM (photoemission electron microscopy) imaging with high lateral resolution provides an experimental tool to look into such phenomena. Owing to the excellent time structure of Synchrotron radiation and pulsed laser sources, high time resolution can be achieved in stroboscopic PEEM imaging. In the ***picosecond to nanosecond range*** remagnetisation processes and transient domain states [1] or magnetic high-frequency eigenmodes in confined magnetic structures [2-4] attract much attention due to challenging applications, e.g. in spintronics. In the ***femtosecond range*** the lifetime contrast of "hot electrons" [5], the properties of plasmon-enhanced optical near fields [6] or the dynamics of surface plasmons are directly accessible by time-resolved PEEM. In a Mach-Zehnder like all-optical pump probe set-up, a temporal precision of 50 attoseconds has been achieved by Kubo et al. [7].

In this contribution the state of the art of time-resolved PEEM is discussed with emphasis on two classes of applications, i.e. imaging of fast magnetization processes and femtosecond electron dynamics. In particular, we focus on stroboscopic imaging of precessional magnetic excitations via XMCD-PEEM exploiting the time-structure of Synchrotron radiation (magnetic field pulse pump – X-ray probe). The method is illustrated in Fig.1. In a special bunch-compression mode at the storage ring BESSY (Berlin), a time resolution of about 15 ps has been obtained. Further, we discuss recent PEEM experiments using femtosecond laser excitation. A current overview on time-resolved PEEM can be found in a forthcoming review [8].

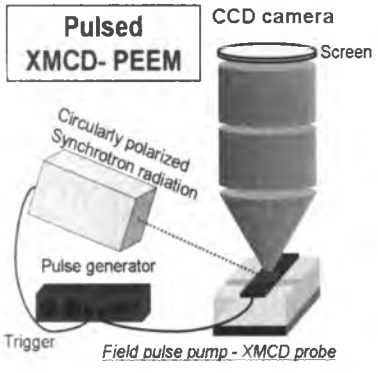

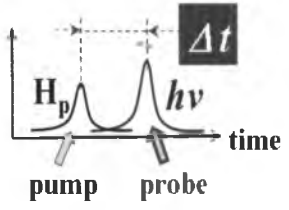

Fig. 1. Schematic view of the experimental set-up (left) and principle of stroboscopic imaging (right). Hp denotes the field pulse (pump), hν the photon pulse (probe).

2. Time-resolved imaging of spin wave eigen-modes in confined systems

In the set-up of Fig.1 the PEEM detects the spatial distribution of the X-ray absorption via the electron yield of secondary electrons. When the energy of circularly polarized photons is tuned to the L_3 absorption edges of a magnetic element, the electron yield varies with the relative orientation of magnetization $\boldsymbol{M}$ and (circular) polarization vector $\boldsymbol{P}$. X-ray magnetic circular dichroism (XMCD) images are obtained from two images taken with opposite photon helicity calculating the asymmetry at each pixel, which is proportional to $\boldsymbol{M} \cdot \boldsymbol{P}$. Fig. 2 shows results for Permalloy ($Ni_{80}Fe_{20}$) platelets with 16 μm width, 32 μm length, and 10 nm thickness, placed on a coplanar waveguide. At grazing incidence we are most sensitive to the in-plane magnetization component along the short side of the platelet.

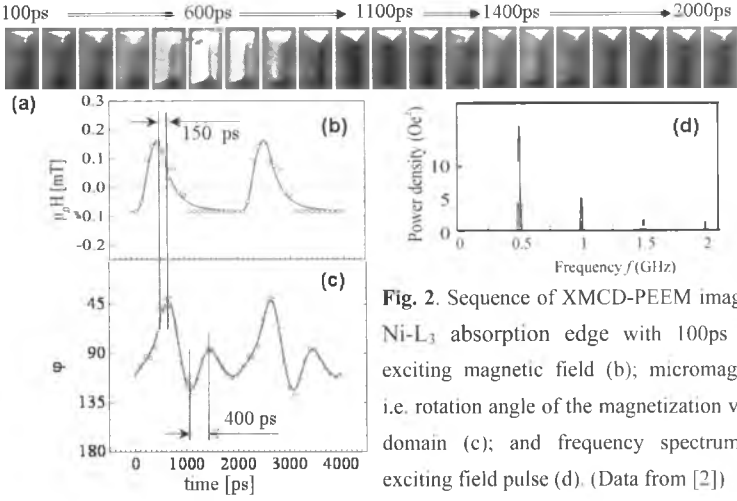

Fig. 2. Sequence of XMCD-PEEM images taken at the Ni-L_3 absorption edge with 100ps increment (a); exciting magnetic field (b); micromagnetic response, i.e. rotation angle of the magnetization vector in the left domain (c); and frequency spectrum (FT) of the exciting field pulse (d). (Data from [2])

A microwave pulse generator injects a high-frequency *ac* current into the waveguide thus generating the magnetic field as shown in Fig. 2b. Time-resolved images are taken by stroboscopic illumination of the sample by X-ray pulses produced by electron bunches in the synchrotron ring (t_{FWHM} = 3 ps, low-alpha mode) with a repetition rate of 500 MHz. The *ac* driving current and the probe pulses are synchronized via a variable electronic delay. Snapshots of the time evolution of the magnetization $\boldsymbol{M}$ in the Permalloy platelet are shown in Fig. 2a. The domains oriented parallel and antiparallel to $\boldsymbol{P}$ appear white and black, while the two domains oriented perpendicular to $\boldsymbol{P}$ both appear gray. An 180^0-Neél wall separates the two large domains with $\boldsymbol{M}$ upward (left) and downward (right). The intensity in the two large domains varies periodically, indicating the predominant excitation mode of a precession of the magnetization around the effective field axis directed parallel to the long side of the platelet. The dynamical response as depicted in Fig. 2c obviously does not follow the field pulse in a trivial way. Instead, the system resembles a driven oscillator, and we observe the dynamical answer to the periodic excitation. The domain walls and, particularly, the 180^0-Neél wall move only very little throughout the series shown in Fig. 2. However, we observe a mean shift of the central wall out of its symmetrical position to the right. This shift increases with increasing amplitude of the exciting field and finally the Neél wall vanishes for large enough amplitudes (see Fig. 3).

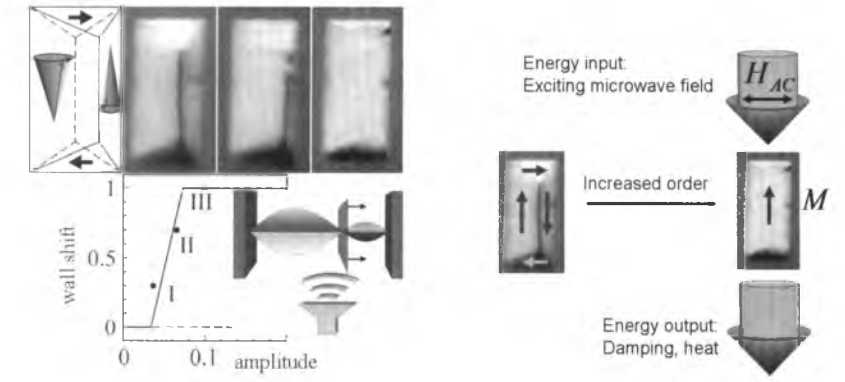

Fig. 3 Left: Sketch and snapshots of magnetic domain patterns at the time $t = 0$ excited with increasing field amplitudes I, II and III. The bottom panel shows comparison of an analytical model and experimentally observed mean shift of the central domain wall. The inset shows an analog mechanical model. **Right:** Within a closed system, entropy maximization increases disorder. An open system with constant energy dissipation allows for an ***increase*** of local order. (Data from [2])

The magnetization distribution adapts itself to increase the energy dissipation and thus causes an overall increase of local order. The near-resonance spin wave mode causes an effective force perpendicular to the 180^0-Neél wall that is balanced by the restoring force of the stray field energy. The system is excited with a significant oscillating field component of 1 GHz (cf. Fig. 2d), i.e., just below the resonance frequency of the free running system of about 1.25 GHz. If the domain wall shifts to the right, the resonance frequency will decrease in the left domain; therefore the amplitude (and the total energy) of the precession will increase in the left domain.

3. Observation of optical near fields and plasmon eigen-oscillations

In experiments using all-optical fs-laser excitation the delay between pump and probe pulse can be generated in a Mach-Zehnder interferometer like element. Thus, any electronic jitter is avoided and the time resolution is finally limited by the properties of the laser pulses. In phase-averaging experiments the resolution is of the order of the pulse lengths (about ten to several tens of fs). In interferometric experiments the *precision* can be driven down to 50 attoseconds [7] (the exciting and probing waves still consist of several periods). Kubo et al. have clearly demonstrated changes of interferometric time-resolved PEEM images on a time scale of 133 attoseconds. Femtosecond-laser excited PEEM also gives access to "hot-electron" dynamics [5] and to plasmon-enhanced optical near fields [6]. An example is shown in Fig. 4. Upon excitation with femtosecond laser pulses at 400 nm, a Ag crescent fabricated on a Si surface does not appear in its true shape, but instead the spatial distribution of the optical near field becomes visible (b). A simulation reveals strong enhancement of the optical near field at 400 nm (e), i.e. the crescent acts as a resonant "nano-antenna" tailored for maximum response at 400 nm excitation. In contrast to SNOM, the PEEM technique does not influence the near field structure.

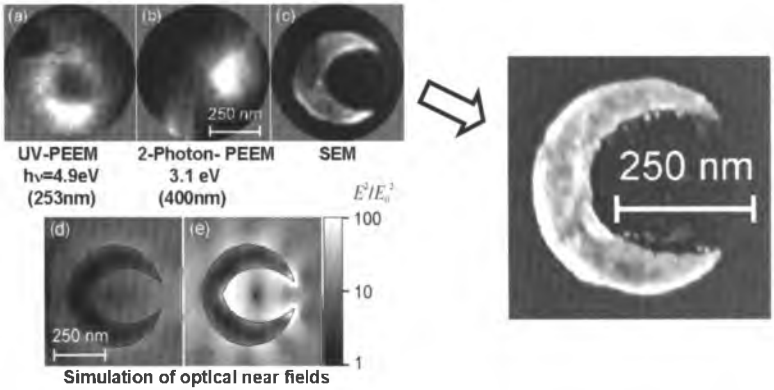

Fig. 4. UV-PEEM image (a) compared with a femtosecond-laser excited two-photon-PEEM image (b) of the identical field of view of a Ag crescent (on Si) shown in the SEM image (c). Strong enhancement of the optical near field at 400 nm (e) as compared to 253 nm (d) is visible in the simulation. (From [6])

In conclusion, time-resolved PEEM is a novel imaging technique with very high potential and with a time resolution that depends essentially on the quality of the photon source. A highly promising alternative to stroboscopic imaging is an approach using *time-resolving image detection*. The delayline detector is particularly useful because it acquires single electron events that are stored in a 3D (x,y,t) histogram memory. Its time resolution is presently about 120 ps and will be improved by about a factor of two (www.surface-concept.de).

References / Acknowledgment

[1] G. Schönhense et al., Nuel. Instr. Meth. B **246** (2006) 1-12
[2] A. Krasyuk et al., Phys. Rev. Lett. **95** (2005) 207201
[3] S.-B. Choe et al., Science **304** (2004) 420
[4] J. Raabe et al., Phys. Rev. Lett. **94** (2005) 217204
[5] O. Schmidt et al., Appl. Phys.B **74** (2002) 223
[6] M. Cinchetti et al., Phys. Rev. Lett. **95** (2005) 047601
[7] A. Kubo et al., Nano Letters **5** (2005) 1123
[8] G. Schönhense et al., in "Advances in Imaging and Electr. Physics", ed. by P. Hawkes, 2006

Thanks are due to A.Krasyuk, M.Cinchetti, H.J.Elmers, S.A.Nepijko, A.Oelsner (Univ. Mainz), C.M. Schneider (FZ Jülich), and M.Kreiter (Max Planck Institute for Polymer Research, Mainz) for excellent cooperation as well as to the BESSY staff for good beamline support. Project funded by BMBF 03N6500.

USE OF A 'FOIL CORRECTOR' IN A MULTIBEAM SOURCE: CORRECTION OF OFF-AXIS MACROLENS ABERRATIONS

M. J. van Bruggen, B. van Someren, P. Kruit

Delft University of Technology, Faculty of Applied Sciences, Particle Optics Group
Lorentzweg 1, 2628 CJ Delft, The Netherlands

We present a multibeam source (MBS) based on splitting the broad beam of a Schottky Field Emission source into many sub-beams with a microlens array (see fig. 1). To avoid problems associated with skewed incidence in the microlenses we use an electrostatic collimator lens to illuminate the microlens array with a parallel beam. However, this collimator lens introduces unacceptably high deflection aberrations. We show that it is possible to create a negative lens in that MBS with negative spherical and chromatic aberration coefficients. This lens can be used to correct the off-axis aberrations of the collimator lens. The MBS will be mounted in a Scanning Electron Microscope (SEM) to produce multiple 1 nm beams. This multibeam SEM will be used as an Electron Beam Induced Deposition nanolithography machine [1].

In 1947 Scherzer published his ideas about a foil corrector that could be used to correct for both spherical and chromatic aberration in electron optical systems [2]. However, the scattering of the electrons in the foil was a serious problem. That difficulty can be circumvented by using a silicon wafer with holes in it that are much smaller than the diameter of the macro electrode in front of it (see fig.2). In our case, we use the aperture lens effect in these holes to focus each sub-beam individually, while the negative macrolens can be used to compensate for the off-axis aberrations introduced in the collimator lens. This silicon microlens array, electrode number 3 in fig. 2, is fabricated with Micro Electro Mechanical System (MEMS) technology with sub-micron accuracy.

The configuration in fig. 1 is modeled using a thin-lens approximation with only one first and third order coefficient for each macrolens, describing the deflection angle at that lens:

$$\Delta\alpha = a_1 h + a_3 h^3 + O(h^5)$$

Here a_1 is the lens strength and a_3 the coefficient describing the third order geometrical aberration from the perfect lens effect; h is the height of incidence in the lens. In fig. 3 it is shown that the a_3 coefficient of the negative lens can be negative, depending on the distance between electrode 3 and 4.
With this model, expressions were found for the shifts in the two perpendicular directions in the paraxial image plane, separated in powers of h. This results in the Seidel aberrations with their coefficients expressed in terms of the single third order coefficient a_3. We expect that this approximation is valid as long as we use the model to see if there is an optimum setting at which both the third order geometrical aberration and the first order chromatic aberration, also taken into account in our model, of the two macrolenses exactly cancel. A full 3D field calculation and ray tracing of the configuration at the optimum setting will be necessary to check the validity of the model.

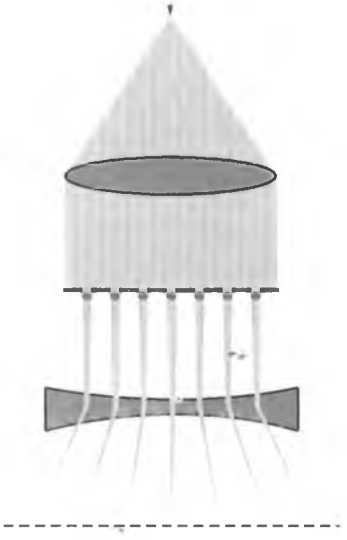

Figure 1. Schematical overview of the proposed multi beam source with a collimator lens, current-limiting aperture array, microlens array and negative lens.

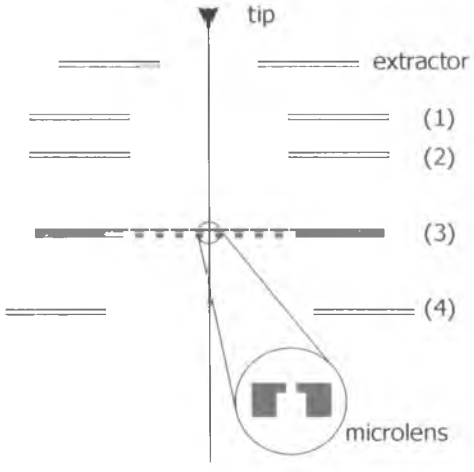

Figure 2. Electrode configuration of the MBS. Element 1 is used to collimate the broad beam, number 2 is on the same potential as the combined current-limiting aperture and microlens array (3) and shields the current-limiting apertures from the lens field of the collimator. The field between electrode 3 and 4 establishes a microlens array and a negative lens at the respective electrodes.

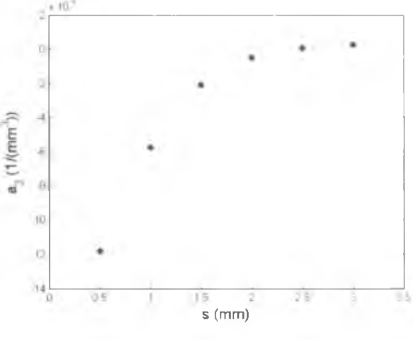

Figure 3. 3-order coefficient a_3 of the negative macrolens as a function of the distance s between electrode 3 and 4 (V_3 = 2.0 kV, V_4 = 4.4 kV and the diameter of electrode 4 is 4 mm).

[1] Bruggen, M.J. van; Someren, B. van; Kruit, P.; Development of a multi-electron-beam source for sub-10 nm electron beam induced deposition, J. Vac. Sci. & Technol. B, 23(6), Nov/Dec 2005.

[2] Scherzer, o.; Sphärische und chromatische Korrektur von Elektronen-Linsen, Optik, 2:114, 1947.

DETECTION OF SIGNAL ELECTRONS IN THE LOW VOLTAGE SEM

P. Wandrol and I. Müllerová

Institute of Scientific Instruments ASCR, Brno, Czech Republic; wandrol@isibrno.cz

In the low voltage SEM (LV SEM) specific approach to the signal detection is needed. As usually, secondary electrons (SE) can be detected by the Everhart-Thornley detector situated in the specimen chamber or inside the final lens. However, energy of BSE is too low to produce a high quality image with standard scintillation or solid state detectors, and it is too high to allow for efficient extraction with a lateral electric field. Some of newest in-lens BSE detectors employ transformation to SE3 [1] or acceleration toward a scintillation detector [2].

Most efficient BSE detector for the primary beam energy 5 keV and higher is the YAG single crystal scintillation detector [3]. Low energy BSEs do not generate the number of photons sufficient for quality image - before they hit the scintillator, acceleration of them to at least 5 keV is necessary. Acceleration is carried out toward a positively biased electrode, which is formed by a thin layer of the indium-tin oxide (ITO), deposited on the scintillator. This layer is transparent for BSE and represents a high-voltage electrode at a potential up to 8 kV. Naturally, the electric field accelerates the secondary electrons, too, so an energy filter at a negative potential of hundred volts is placed between the specimen and scintillator. A grounded tube inserted in the scintillator bore shields the primary electron beam, and the entire scintillator is surrounded with a grounded shielding as well. Schematic view of the improved BSE detector for LV SEM applications is shown in Fig. 1.

The detector has been installed in the specimen chamber of a field emission SEM with an immersion objective lens. In this microscope, secondary electrons move on helical trajectories, being collimated into the final lens. This has been revealed by computer simulation of the spatial distribution of fields as well as of the signal electron trajectories [4], performed by means of software packages MLD, ELD and Trasys [5]. We have found that not all SEs reach the final lens and 10 to 20 % of them can hit the scintillator of BSE detector. The proportion depends on the SE energy and emission angle. Computer simulations have been confirmed by experimental results that showed essential the application of the energy filter. Difference between signals acquired with the energy filter grounded or negatively biased is demonstrated by images of a blast furnace slag sample in Figs. 2 and 3. With energy filter grounded, a mixture of SE and BSE is collected (Fig. 2). Combined topographical and compositional contrast with dominance of the topographical one is obvious here because the SE yield at low energies is several times higher than the BSE yield. Only BSEs are collected when applying -200 V bias on the energy filter. Then the distribution of metal oxides in the slag is clearly visible (Fig. 3). In both cases the high voltage electrode on the scintillator is biased to +4.5 kV. Fig. 4 presents the signal levels measured on a gold surface – the characteristic energy dependences of SE and BSE yields are here appearing as limiting cases.

The detector can be retracted off the optical axis in order to suppress the impact of BSE and to detect preferably the secondary electrons. For efficient collection of SE, the energy filter must have a positive bias of hundreds volts (Fig. 5).

The above-described detector offers a solution to the BSE problem in the LV SEM mode for every scanning electron microscope. Signal of this detector is approximately three times larger in comparison with a standard YAG-crystal BSE detector at accelerating voltages from 0.5 to 3 kV. Besides detection of low energy BSE, this type enables one to detect also the SE signal and an SE+BSE signal mixture.

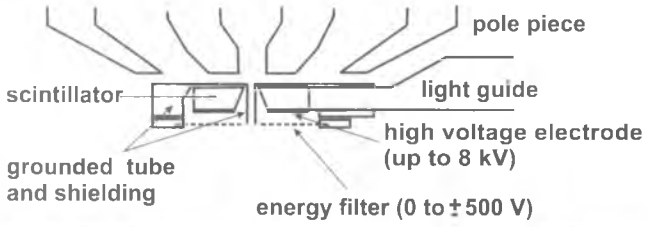

Fig. 1. Scintillation type BSE detector for low acceleration voltage application.

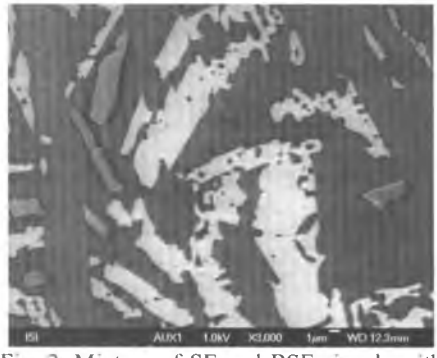

Fig. 2. Mixture of SE and BSE signals with the energy filter grounded; the high voltage electrode at 4.5 kV.

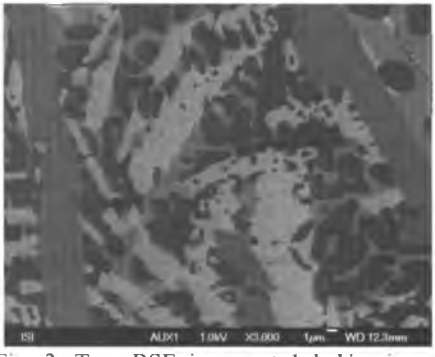

Fig. 3. True BSE image at 1 keV primary beam; the energy filter biased to -200 V, the high voltage electrode at 4.5 kV.

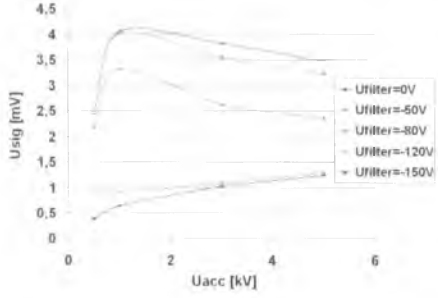

Fig. 4. Output signal from the detector, plotted versus the accelerating potential.

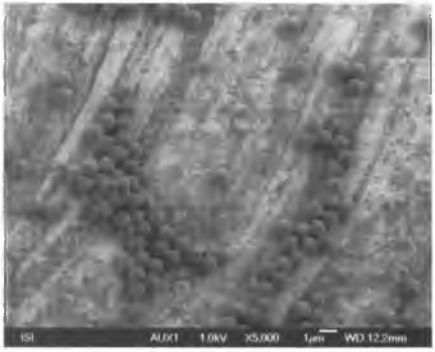

Fig. 5. An SE image of uncoated polystyrene latex spheres acquired by the BSE detector. Bias of the energy filter is +300 V, the high voltage electrode is at 4.5 kV.

[1] Hitachi Scientific Instrument Technical Data, sheet no. 98, see http://www.hitachi-hta.com/pageloader~type~page~id~emd_tech_notes.html.
[2] Steigerwald M. G. D., Microscopy Today **11** (2003) 26.
[3] Autrata R., Hermann R., Müller M., Scanning **14** (1992) 127.
[4] Wandrol P., Autrata R., in Proc. Recent Trends 2004 (2004) 77.
[5] Lencová B., Wisselink G., Nucl. Instrum. Meth. **A298** (1990) 56.
[6] The work is supported by the Grant Agency of ASCR under grant no. KJB200650501.